JOHANNES KEPLER UNIVERSITY LINZ

Institute of Computational Mathematics

Viscoplastic Models and Finite Element Schemes for the Hot Rolling Metal Process

Ioannis Toulopoulos
AC2T Research GmbH
Austrian Excellence Center for Tribology
Viktor-Kaplan-Straße 2/C, 2700 Wiener Neustadt, Austria
and
Institute of Computational Mathematics, Johannes Kepler University
Altenberger Str. 69, 4040 Linz, Austria

NuMa-Report No. 2020-01 Februay 2020

A–4040 LINZ, Altenbergerstraße 69, Austria

Technical Reports before 1998:

1995

95-1	Hedwig Brandstetter *Was ist neu in Fortran 90?*	March 1995
95-2	G. Haase, B. Heise, M. Kuhn, U. Langer *Adaptive Domain Decomposition Methods for Finite and Boundary Element Equations.*	August 1995
95-3	Joachim Schöberl *An Automatic Mesh Generator Using Geometric Rules for Two and Three Space Dimensions.*	August 1995

1996

96-1	Ferdinand Kickinger *Automatic Mesh Generation for 3D Objects.*	February 1996
96-2	Mario Goppold, Gundolf Haase, Bodo Heise und Michael Kuhn *Preprocessing in BE/FE Domain Decomposition Methods.*	February 1996
96-3	Bodo Heise *A Mixed Variational Formulation for 3D Magnetostatics and its Finite Element Discretisation.*	February 1996
96-4	Bodo Heise und Michael Jung *Robust Parallel Newton-Multilevel Methods.*	February 1996
96-5	Ferdinand Kickinger *Algebraic Multigrid for Discrete Elliptic Second Order Problems.*	February 1996
96-6	Bodo Heise *A Mixed Variational Formulation for 3D Magnetostatics and its Finite Element Discretisation.*	May 1996
96-7	Michael Kuhn *Benchmarking for Boundary Element Methods.*	June 1996

1997

97-1	Bodo Heise, Michael Kuhn and Ulrich Langer *A Mixed Variational Formulation for 3D Magnetostatics in the Space* $H(rot) \cap H(div)$	February 1997
97-2	Joachim Schöberl *Robust Multigrid Preconditioning for Parameter Dependent Problems I: The Stokes-type Case.*	June 1997
97-3	Ferdinand Kickinger, Sergei V. Nepomnyaschikh, Ralf Pfau, Joachim Schöberl *Numerical Estimates of Inequalities in* $H^{\frac{1}{2}}$.	August 1997
97-4	Joachim Schöberl *Programmbeschreibung NAOMI 2D und Algebraic Multigrid.*	September 1997

From 1998 to 2008 technical reports were published by SFB013. Please see
`http://www.sfb013.uni-linz.ac.at/index.php?id=reports`
From 2004 on reports were also published by RICAM. Please see
`http://www.ricam.oeaw.ac.at/publications/list/`
For a complete list of NuMa reports see
`http://www.numa.uni-linz.ac.at/Publications/List/`

Viscoplastic models and finite element schemes for the hot rolling metal process

Ioannis Toulopoulos[1,2]

[1] AC2T Research GmbH, Austrian Excellence Center for Tribology,
Viktor-Kaplan-Straße 2/C, 2700 Wiener Neustadt, Austria,

[2] Institute of Computational Mathematics, Johannes Kepler University (JKU),
Altenberger str. 69, A-4040 Linz, Austria,

Ioannis.Toulopoulos@ac2t.at

Abstract. In this work, pure viscoplastic models and their finite element discretization employed for the hot rolling method of plate metal forming are discussed. The derivation of the viscoplastic flow rule and the relation between the stress-strain rates are presented. The associated equilibrium system of the deformation problem is completed by describing the form of the inlet/outlet boundary conditions as well as by introducing the contact conditions and a viscoplastic friction law. The system is discretized using the continuous finite element method where classical penalty terms are used for incorporating the boundary conditions and the contact conditions. The use of a viscoplastic friction law requires an estimation of the friction parameter which is obtained through the derivation of stability estimates for the finite element scheme. Numerical tests are performed and their results compared in order to investigate the effect of the strain sensitivity parameter on the behavior of the plate velocity and on the magnitude of the interfacial stresses

Key words: hot rolling, metal forming, pure viscoplastic models, Norton-Hoff laws, contact-friction interface conditions, finite element discretizations, friction parameter, boundary constraints, penalty terms

1 Introduction

In recent years, there has been a growing interest in the use of accurate mathematical models and numerical methods for describing and simulating the rolling metal forming process, i.e., the process of the plastic deformation of a metal plate passing through a pair of rotating rolls, [10], [13], [16], [17], [18]. During the rolling process, the thickness (height) of the metal plate is decreased while its length is increased. The rolling technique for metal forming involves many phenomena such as nonlinear plastic deformation behavior, large strain rates and depends mainly on the friction and contact boundary conditions. The development of efficient and accurate finite element methods for studying these problems is an interesting subject that has attracted many scientists.

In the work [37], viscoplastic models were used and the frictional stresses were computed using a thin layer of elements across the interface. An investigation using rigid-plastic finite element methods and employing different friction laws in the rolling process of metal forming was carried [19], and in a later work [12], rigid-plastic models were used including the variation of the rolling coefficient across the interface. In the study presented in [25], viscoplastic strain-stress relations were applied by assuming two different friction models. A series of numerical tests were performed for computing the tangential and normal stress on the interface points. In recent years, other kind of models and many other different finite element methodologies have been proposed. Mesh free finite element methods for slightly compressible rigid-plastic models have been applied for simulating plane strain rolling problems in [34]. Hybrid Eulerian-Lagrangian finite element formulations for discretizing rigid viscoplastic models have been discussed in [27] and [29]. In [27], a numerical investigation of the rolling problem was presented by performing several tests using different values for the radius and the velocity of the rollers. In the recent work [30], elastoplastic-models and Augmented Lagrangian techniques have been used for discretizing the contact and the frictional conditions. In addition, the authors proposed an optimal control problem for achieving the desired shape of the plate. Rigid-plastic finite element schemes with efficient and fast nonlinear solvers were developed and analysed in [35].

The motion of the plate is mainly governed by two equations, the constitutive equation and the continuum equilibrium equation. The constitutive equation provides a relationship between the stress and strain rate (deformation rate) [24], [2], [31]. In many metal forming processes, the elastic effects are weak and viscoplastic constitutive relations are introduced for describing the problem, which lead to an Eulerian descriptions with the velocity components as the unknowns. Here, we consider a pure viscoplastic (Norton-Hoff) model, such that the constitutive equation has the form $\boldsymbol{\sigma} = a(\dot{\varepsilon}_{vp})\dot{\boldsymbol{\varepsilon}}$ where $\boldsymbol{\sigma}$ is the stress tensor, $\dot{\varepsilon}_{vp}$ is the effective viscoplastic strain rate, $a(t) = t^{m-1}$, $m > 0$ is a power law function, and $\dot{\boldsymbol{\varepsilon}}$ is the strain rate tensor. In our model, the inertia effects are ignored. This constitutive equation is similar to the non-Newtonian fluid flow problems [7] and helps in relating the stress components to the strain-rate components. The associated formulation allows a direct imposition of the plastic flow incompressibility constraint, i.e., the divergence free condition of the velocity field, [6], [10].
The equilibrium system formulates the balance between the external and the internal forces. The finite element discrete analog of the equilibrated equations results in a (nonlinear) system, with the velocity and the pressure on the nodal mesh points, which are functions of time, as the unknown quantities. Having computed the solution for the system, we can update the configuration using an explicit time-stepping scheme. Finite element schemes for flow formulations were presented with different time-stepping schemes for thin-sheet-forming processes in previous studies, see, e.g., [23], [36].
As mentioned above, the rolling deformation process is a complicated problem and cannot be treated easily via numerical calculations, even though the whole numerical computation is driven to a steady-state. One reason for this is the strong nonlinearities that appear in the model. Apart from the nonlinear terms that appear in the constitutive law, nonlinear inequality constraints also arise on the contact interface due to the imposition of bilateral contact conditions (non-penetration constraint) and due to form of the friction laws. Another reason is related to the changing of the contact interface points. The contact interface is not constant and pre-defined, but changes with the time evolution of the problem since the plate moves between the rollers. Consequently, after every time step, we need to re-determine the contact interface and the points that live on it. We note that the points located before the entrance of the roller gap are moving with a lower velocity than the rollers, while the points after the roller gap are moving with higher velocity. This change of the plate velocity brings about analogous inlet/outlet boundary constraints (inequalities). Different techniques exist for incorporating these boundary constraints. Here, we employ the penalty term technique [21], [9]. Furthermore, due to the velocity change of the plate, the tangential friction stresses, $\mathbf{T}_\tau$, change direction. The location of the neutral point, where the relative velocity between the tangential plate and the roll are equal, i.e., the point where $\mathbf{T}_\tau$ changes direction, is not a priori known. However, it "moves" through the initial time steps and finally becomes fixed during the steady-state computations.
Another important point in rolling problems is the modeling (and discretization) of the interfacial friction phenomena between the rollers and the metal plate. Due to the complexity of the rolling process, simplified friction laws, such as Coulomb's law, are not appropriate and thus, more advanced friction laws must be used for obtaining accurate results (see, e.g., [5] and the references therein). The use of an appropriate friction law is important for simulating the problem because the friction forces play a crucial role in driving the metal plate into the roller gap and consequently influences the behavior of the deformed plate. In this work, viscoplastic type friction laws are used which are compatible with the viscoplastic constitutive equation (see the form of the friction stress vector $\mathbf{T}_\tau$ in (2.29a)). These types of laws have been used in many works, showing better results compared to other more classical friction laws (see [5], [20]).
We apply a continuous finite element method for the discretization of the problem, where the interface friction conditions are consistently adapted in the discrete variational form. The boundary and the non-penetration constraints are enforced by introducing penalty terms. For this, we construct a set of nonlinear penalty functions that are added in the equilibrium system and are

activated when the inequality constraints are not satisfied [9]. The convergence properties of these penalty terms are not investigated in this work.
The neutral point is a singular point for the viscoplastic friction law and simple regularization techniques are applied by adding a small perturbation constant in the friction law. In order to compute the tangential friction stresses, it is necessary to estimate the value of the associated friction parameter (denoted by a_f in (2.29a)). For some simplified problems, laboratory experiments can usually provide a good estimation of this parameter. In general, its value depends on several quantities such as temperature, surface roughness, material properties, etc. Specific results on the estimation of the friction parameter for hot rolling are difficult to obtain due to the nature of the rolling process [5]. In the current work, an estimation formula of the parameter is provided through a proof of giving stability bounds for the problem. In the numerical examples, the coefficient a_f is computed at every time step using this estimate. The new update is used for the next time step computation.
A numerical investigation of the rolling process is presented by performing an extensive series of numerical simulation tests. We investigate the variations of the relative velocity and the values of the normal/tangential stresses with respect to the sensitivity strain parameter.

The remainder of this paper is outlined as follows: the derivation of the viscoplastic constitutive law is discussed in Section 2. Issues related to the variational formulation of a simple deformation problem and the contact-friction conditions are also discussed in Section 2, thus preparing all the necessary concepts required for modeling the rolling problem, which is given in Section 3. The procedure of finite element discretization along with the steps followed for estimating the friction parameter are also given in this section. Several numerical tests performed for a numerical study of the rolling problem are presented in Section 4. The paper closes with the conclusions given in Section 5.

2 The model problem

2.1 Preliminaries

We use a standard notation throughout this work. Let Ω be a bounded Lipschitz domain in $\mathbb{R}^d$, $d = \{2,3\}$. For a differentiable function $\phi : \Omega \to \mathbb{R}$ the gradient at $x = (x_1, \ldots, x_d)$ is the vector $\nabla\phi(x) = \big(\frac{\partial\phi(x)}{\partial x_1}, \ldots, \frac{\partial\phi(x)}{\partial x_d}\big)$. We denote by $L^p(\Omega)$, $p > 1$, the Lebesgue space of measurable functions $\phi : \Omega \to \mathbb{R}$ such that $\int_\Omega |\phi(x)|^p\,dx < \infty$ endowed with the norm $\|\phi\|_{L^p(\Omega)} = \big(\int_\Omega |\phi(x)|^p\,dx\big)^{\frac{1}{p}}$. Let $\alpha = (\alpha_1, \ldots, \alpha_d)$ be a multi-index of non-negative integers $\alpha_1, \ldots, \alpha_d$ with degree $|\alpha| = \sum_{j=1}^d \alpha_j$. For any α, we define the differential operator $D^\alpha = \partial/\partial x_1^{\alpha_1} \ldots \partial/\partial x_d^{\alpha_d}$, and denote the standard Sobolev spaces by

$$W^{\ell,p}(\Omega) = \{\phi \in L^p(\Omega) : D^\alpha\phi \in L^p(\Omega), \text{ for all } |\alpha| \le \ell\}, \tag{2.1}$$

endowed with the following norms

$$\|\phi\|_{W^{\ell,p}(\Omega)} = \Big(\sum_{0\le|\alpha|\le\ell} \|D^\alpha\phi\|^p_{L^p(\Omega)}\Big)^{\frac{1}{p}}.$$

where the derivatives in (2.1) are considered in the weak sense. The definition of the spaces in (2.1) is naturally extended to the vector value functions $\boldsymbol{\phi} = (\phi_1, \ldots, \phi_d)$. For simplicity, we denote the associated spaces by $\mathbf{W}^{\ell,p}$. We refer to Ref. [1] for a complete description of the Sobolev spaces. For a later use, we define the vector space

$$\boldsymbol{\mathcal{V}} := \mathbf{W}^{\ell,p}(\Omega), \text{ with } \ell \ge 1, p = m+1, \tag{2.2}$$

where m is the exponent parameter in the viscoplastic model, see (2.20).
Let $p > 1$, we define its conjugate q by the relation $\frac{1}{p} + \frac{1}{q} = 1$. We recall Hölder's and Young's inequalities

$$\left| \int_{\Omega} \phi_1 \phi_2 \, dx \right| \leq \|\phi_1\|_{L^p(\Omega)} \|\phi_2\|_{L^q(\Omega)} \quad \text{and} \quad \left| \int_{\Omega} \phi_1 \phi_2 \, dx \right| \leq \frac{\epsilon}{p} \|\phi_1\|^p_{L^p(\Omega)} + \frac{1}{q\epsilon} \|\phi_2\|^q_{L^q(\Omega)}, \tag{2.3}$$

that hold for all $\phi_1 \in L^p(\Omega)$ and $\phi_2 \in L^q(\Omega)$ and for any fixed $\epsilon \in (0, \infty)$, [1]. We shall use the summation convection, according to which repeated indices indicate a summation from 1 up to the dimension of the involved vectors. We will frequently use the double contracted product between tensors, namely $A : B = \sum_{i,j} A_{ij} B_{ij}$, which results in a scalar. The double contracted product defines an inner product between tensors.

2.2 Notations

Let the set $\Omega \subset \mathbb{R}^d$, $d \in \{2, 3\}$ be the (reference) configuration of a body consisting of a viscoplastic material. We are interested in describing the deformation of the body subjected to body forces $\mathbf{f}$ and surface tractions, $\mathbf{T}$, which are applied to a part of the body surface. As usual the displacement of each point $\mathbf{x} \in \Omega$ is denoted by $\mathbf{u} = (u_1, \ldots, u_d)$ and the components ε_{ij} of the linear (infinitesimal) strain tensor $\boldsymbol{\varepsilon}$ produced by $\mathbf{u}$ are given by $\varepsilon_{ij} = \frac{1}{2}(\frac{\partial u_i}{\partial x_j} + \frac{\partial u_j}{\partial x_i})$, with $1 \leq i \neq j \leq d$. The components of the velocity $\mathbf{v} = (v_1, \ldots, v_d)$ of the material points at a certain time t are defined by $v_i = \frac{\partial u_i}{\partial t}$ and the components of the strain rate tensor $\dot{\boldsymbol{\varepsilon}}$ are given by

$$\dot{\varepsilon}_{ij} = \frac{1}{2}\left(\frac{\partial v_i}{\partial x_j} + \frac{\partial v_j}{\partial x_i}\right), \text{ with } 1 \leq i \neq j \leq d. \tag{2.4}$$

Here we suppose, see next sections, that there exist a viscoplastic potential $\varphi := \varphi(\dot{\boldsymbol{\varepsilon}})$ such that the stress-strain constitutive relations can be derived by

$$\sigma_{ij} = \frac{\varphi(\dot{\boldsymbol{\varepsilon}})}{\partial \dot{\varepsilon}_{ij}}, \tag{2.5}$$

where σ_{ij} are the components of the stress tensor $\boldsymbol{\sigma}$. In the deformation problems here the hydrostatic pressure has very little effect and the strain rates and the associated stresses are deviatoric. We introduce the deviatoric stress tensor $\mathbf{s} := \boldsymbol{\sigma} + P\mathbf{I}$ with $P = \frac{1}{d} trace(\boldsymbol{\sigma})$, which has a trace equal to 0 and the same principal directions as $\boldsymbol{\sigma}$. Also, we note that we consider small strain cases and the linear strain tensor can be split into an elastic part $\boldsymbol{\varepsilon}_e$ and a plastic part $\boldsymbol{\varepsilon}_p$, i.e., $\boldsymbol{\varepsilon} = \boldsymbol{\varepsilon}_e + \boldsymbol{\varepsilon}_p$.

2.3 Plasticity criterion and stress-strain relations

It is known from the studies of small strain plasticity problems [4], that the materials after being subjected to a stress σ beyond the yield stress σ_0, they have plastic deformation behavior, which means that permanent deformations of the material exist when we return back to the unstressed state. The behavior of the materials before reaching the yield stress point σ_0 is elastic without the evolution of plastic strains. In a general situation when a stress tensor $\boldsymbol{\sigma}$ is defined on a point $\mathbf{x}$ of the material, we would like to have a criterion in order to verify if the related stresses are below σ_0 (elastic region) or above σ_0 (plastic region). Mathematically this means that we need to formulate an inequality constraint that will depend on the stresses σ and σ_0. Below we give this inequality and also derive the basic equations in plasticity, i.e., yield condition, flow rule, stress-strain relation, following the von Mises viscoplasticity framework, see e.g., [2], [4], [26]. Let us consider the principal - axial stress case for $d = 3$ and define

$$J_2 = \frac{1}{2} s_{ij} s_{ij}, \tag{2.6}$$

where s_{ij} are the components of $\mathbf{s}$ defined by

$$\mathbf{s} = \begin{pmatrix} \ldots & & 0 \\ 0 & & \sigma_{ii} - \dfrac{1}{3}(\sigma_{11} + \sigma_{22} + \sigma_{33}) \\ 0 & & \ldots \end{pmatrix} \tag{2.7}$$

Using the above relations, we introduce the von Misses plasticity yield function, [4],

$$\Phi(\boldsymbol{\sigma}, \sigma_0) = \big(3J_2\big(\mathbf{s}(\boldsymbol{\sigma})\big)\big)^{\frac{1}{2}} - \sigma_0 := \sigma_{ef} - \sigma_0, \tag{2.8}$$

where we let $\sigma_{ef} := \sqrt{3}\sqrt{J_2(\mathbf{s}(\boldsymbol{\sigma}))}$ to be the effective stress. Based on (2.8), we define the plasticity surface $\mathcal{E} = \{\boldsymbol{\sigma} : \Phi(\boldsymbol{\sigma}, \sigma_0) = 0\}$. A stress $\boldsymbol{\sigma}$ such that $\Phi(\boldsymbol{\sigma}, \sigma_0) < 0$ lies in the elastic domain and for a $\boldsymbol{\sigma} \in \mathcal{E}$ a plastic deformation can occur. We note that here we focus on the solution of purely viscoplastic problems, and hence we neglect the elastic strain component in the additive decomposition of the strain rate tensor $\dot{\boldsymbol{\varepsilon}} = \dot{\boldsymbol{\varepsilon}}_e + \dot{\boldsymbol{\varepsilon}}_p$, i.e., we set $\dot{\boldsymbol{\varepsilon}}_e = 0$.

Having defined the plasticity criterion (2.8), we proceed to express the plastic flow rule, i.e., the particular form of the plastic strain rate tensor $\dot{\boldsymbol{\varepsilon}}_p$. The derivation of the plastic flow rule is based on the principle of the maximum work: given a stress $\boldsymbol{\sigma}$ which verifies the plasticity criterion, $\boldsymbol{\sigma} \in \mathcal{E}$, and its associated strain rate tensor $\dot{\boldsymbol{\varepsilon}}_p$, then for every other stress $\hat{\boldsymbol{\sigma}}$ such that $\Phi(\hat{\boldsymbol{\sigma}}, \sigma_0) \leq 0$, we have

$$\hat{\boldsymbol{\sigma}} : \dot{\boldsymbol{\varepsilon}}_p \leq \boldsymbol{\sigma} : \dot{\boldsymbol{\varepsilon}}_p, \tag{2.9}$$

where the double contracted product between tensors has been used. Based on (2.9), we can conclude that $\dot{\boldsymbol{\varepsilon}}_p$ must be proportional to the exterior normal $\frac{\partial \Phi}{\partial \boldsymbol{\sigma}}$ on the $\mathcal{E}$

$$\dot{\boldsymbol{\varepsilon}}_p = \lambda \frac{\partial \Phi}{\partial \boldsymbol{\sigma}}, \quad \text{or componentwise} \quad \varepsilon_{p,ij} = \lambda \frac{\partial \Phi}{\partial \sigma_{ij}}, \tag{2.10}$$

where the scalar parameter λ determines the plastic rate, for more details we refer to [4],[2].

Note that (2.10) specifies the form of $\dot{\boldsymbol{\varepsilon}}_p$ and the direction of the plastic flow through the term $\dfrac{\partial \Phi}{\partial \boldsymbol{\sigma}}$. By (2.7) we have that

$$\frac{\partial s_{ij}}{\partial \sigma_{mn}} = \begin{cases} \dfrac{d-1}{d} := \dfrac{2}{3} & \text{if } i = j = m = n \\ \dfrac{1}{d} := \dfrac{1}{3} & \text{if } i = j \neq m = n \end{cases}. \tag{2.11}$$

Now recalling (2.8) and that $\sigma_{ef} = \sqrt{\frac{3}{2}}\,\|\mathbf{s}\|$ after performing few computations we can show that

$$\dot{\varepsilon}_{p,ij} = \frac{\partial \Phi}{\partial \sigma_{jj}} = \sum_i \frac{\partial \sigma_{ef}}{\partial s_{ii}} \frac{\partial s_{ii}}{\partial \sigma_{jj}} = \sqrt{\frac{3}{2}} \frac{1}{\|\mathbf{s}\|} \frac{1}{3}(2s_{jj} - \sum_{i \neq j} s_{ii}) = \sqrt{\frac{3}{2}} \frac{s_{ij}}{\|\mathbf{s}\|} := \sqrt{\frac{3}{2}} n_i, \;\; 1 \leq i, j \leq 3, \tag{2.12}$$

where $\mathbf{n} = (n_1, n_2, n_3)$ is the outward normal vector on $\mathcal{E}$, and its principal directions n_i, $i = 1, 2, 3$ coincide with those of $\mathbf{s}$. The flow rule results in

$$\dot{\boldsymbol{\varepsilon}}_p = \lambda \sqrt{\frac{3}{2}} \frac{\mathbf{s}}{\|\mathbf{s}\|} = \lambda \sqrt{\frac{3}{2}} \mathbf{n}, \tag{2.13}$$

and by (2.13) we immediately have that $\lambda = \sqrt{\frac{2}{3}}\|\dot{\boldsymbol{\varepsilon}}_p\| := \dot{\varepsilon}_{ep}$. On the other hand, we have that the stress $\boldsymbol{s}$ satisfies the plasticity criterion (2.8), thus $\sigma_0^2 = \sigma_{ef}^2 = \dfrac{3}{2} s_{ij}\, s_{ij}$, and then by (2.10) and (2.13) we get that

$$\dot{\varepsilon}_{p,ij} = \dot{\varepsilon}_{ep}\sqrt{\frac{3}{2}}\frac{1}{\sqrt{\frac{2}{3}}\sigma_0} s_{ij} = \frac{3}{2}\Big(\frac{\dot{\varepsilon}_{ep}}{\sigma_0}\Big) s_{ij}, \tag{2.14a}$$

or in tensor form

$$\dot{\boldsymbol{\varepsilon}}_p = \sqrt{\frac{3}{2}}\Big(\frac{\|\dot{\boldsymbol{\varepsilon}}_p\|}{\sigma_0}\Big)\mathbf{s}. \tag{2.14b}$$

Remark 2.1. In many metal plasticity models, the history of the plastic deformation must be taken into account. It is usually defined using the effective plastic strain $\varepsilon_{ep} = \int_0^T \dot{\varepsilon}_{ep}(t)\, dt$, where $\dot{\varepsilon}_{ep}$ is the effective plastic strain rate, which is defined in the previous analysis. The effective plastic strain is often used to characterize the inelastic properties of the material, [2], [4].

Remark 2.2. An evolution of the plastic strain rate can be accompanied by an evolution of the strength of the plastic threshold, σ_0. The increase in the plastic threshold after its initial value is called work hardening. The hardening behavior of the material generally depends on the history of the plastic deformation. In this case, σ_0 is taken to be a function of the effective plastic strain, i.e., $\sigma_0 := \sigma_0(\varepsilon_{ep})$ and the plasticity criterion (2.8) takes the form $\Phi(\boldsymbol{s}, \sigma_0) = \sigma_{ef}^2 - \sigma_0^2(\varepsilon_{ep})$. The analytical form of $\sigma_0(\varepsilon_{ep})$ is determined by rheological tests, see the discussion in [22] and [4].

Remark 2.3. As a continuation of Remark 2.2, we note that for the stresses where σ_{ef} is less than the flow stress $\sigma_0(\varepsilon_{ep})$, the behavior of the physical problem is elastic. When the effective stress σ_{ef} reaches the value of $\sigma_0(\varepsilon_{ep})$, the strain rate partly contains a plastic strain rate.

2.4 The viscoplastic constitutive law

It has been well verified through experimental observations that in hot metal plastic deformations the stress-strain relation is appropriately described by using power-law rules, i. e., the stress tensor exhibits a power-law dependence on the strain rate tensor (Norton-Hoff viscoplastic constitutive relations), [10], [24]. In several cases in the derivation and in the further analysis of the models of metal forming problems, the introduction and definition of the plasticity yield surface $\mathcal{E}$, which separates the elastic form the plastic domain, see (2.8), is not necessary. For example, in many metal forging procedures at high temperatures the values of σ_0 are very small, and the metals behave as flowing under week stresses. Consequently we can consider σ_0 to be zero or can neglect σ_0 from the formulation of the model. Thus, Norton-Hoff viscoplastic models with $\sigma_0 = 0$ are widely used, [6], [24], [10]. In their uniaxial form the flow rule is given by

$$\sigma = K\, |\dot{\varepsilon}_p|^m, \tag{2.15}$$

where $K > 0$ is a temperature dependent material parameter and the coefficient $m > 0$ is the strain rate sensitivity coefficient.
We extend the notions of the previous paragraph and denote by $\dot{\boldsymbol{\varepsilon}}_{vp}$ the viscoplastic strain rate tensor and define the effective viscoplastic strain by

$$\dot{\varepsilon}_{vp} = \sqrt{\frac{2}{3}\dot{\varepsilon}_{vp,ij}\dot{\varepsilon}_{vp,ij}} := \sqrt{\frac{2}{3}}\|\dot{\boldsymbol{\varepsilon}}_{vp}\|, \tag{2.16}$$

where the summation convection for the repeated indices has been used. Now the von-Mises based multi-axial generalization of (2.15) has the form, [4]

$$\sigma_{ef} = K\, 3^{\frac{m+1}{2}} \dot{\varepsilon}_{vp}^{\,m}, \tag{2.17}$$

and recalling (2.14) we have that

$$\dot{\varepsilon}_{vp,ij} = \frac{3}{2}\frac{\dot{\varepsilon}_{vp}}{\sigma_{ef}} s_{ij}, \quad \text{or in tensor form} \quad \dot{\boldsymbol{\varepsilon}}_{vp} = \frac{3}{2}\frac{\dot{\varepsilon}_{vp}}{\sigma_{ef}}\mathbf{s}. \tag{2.18}$$

Inserting (2.17) into (2.18) we get

$$\dot{\boldsymbol{\varepsilon}}_{vp} = \frac{3}{2}\frac{\dot{\varepsilon}_{vp}}{K 3^{\frac{m+1}{2}} \dot{\varepsilon}_{vp}^{m}} = \frac{\sqrt{3}^{1-m}}{2K}\dot{\varepsilon}_{vp}^{1-m}\mathbf{s}, \tag{2.19}$$

where we can finally obtain a multidimensional generalization of the Norton-Hoff type viscoplastic constitutive relation given in (2.15)

$$\mathbf{s} = 2\,K\left(\sqrt{3}\,\dot{\varepsilon}_{vp}\right)^{m-1}\dot{\boldsymbol{\varepsilon}}_{vp}. \tag{2.20}$$

It should be noted that, by comparing the models of interest given in (2.14b) and (2.20), it can be seen that the stress multiplier consists of a non-linear function of the effective viscoplastic strain rate $\dot{\varepsilon}_{vp}$, which follows a power-law rule, and essentially relates the stress variations to the strain rate. This multiplier corresponds to a viscosity term, [7], which for $m = 1$ is equal to $2K$ (linear relation). In the numerical computations, the regularized form

$$\mathbf{s} = 2\,K\,\sqrt{3}^{m-1}\left(\varepsilon_0^2 + \dot{\varepsilon}_{vp}^2\right)^{\frac{m-1}{2}}\dot{\boldsymbol{\varepsilon}}_{vp} \tag{2.21}$$

is used for avoiding deviations with very small numbers.

Remark 2.4. We can see by (2.21) that the deviatoric stress tensor $\mathbf{s}$ can be derived by the viscoplastic potential $\varphi := \frac{K}{m+1}(\sqrt{3}\dot{\varepsilon}_{vp})^{m+1}$, i.e., $\mathbf{s} = \frac{\partial\varphi}{\partial\dot{\varepsilon}_{vp}}$, see also (2.5).

2.5 Equilibrium equations

We recall the notations given in Section 2.2, and let Ω denote the bounded domain in the space occupied by a viscoplastic continuum. The boundary $\partial\Omega$ consists of two parts, Γ_D and Γ_N, i.e., $\partial\Omega = \Gamma_D \cup \Gamma_N$, with $|\Gamma_D| > 0$. Let Ω be acted upon by an interior force $\mathbf{f} = (f_1, f_2, f_3)$ and a boundary force $\mathbf{T} = (T_1, T_2, T_3)$ act on Γ_N. On the boundary Γ_D, the displacement $\mathbf{u}$ is fixed, e.g., $\mathbf{u} = 0$, and consequently the point velocity is $\mathbf{v} = 0$. The true internal stresses inside the body are described by the symmetric stress tensor $\boldsymbol{\sigma}$. As mentioned in the previous sections we focus on the problem of incompressible materials (note again that $\mathbf{s} = \boldsymbol{\sigma} + P\mathbf{I}$, with $P := -\frac{1}{d}trace(\boldsymbol{\sigma})$, is deviatoric and $trace(\mathbf{s}) = \operatorname{div}\mathbf{v} = 0$). We recall the vector space $\boldsymbol{\mathcal{V}} = \mathbf{W}^{\ell,p}(\Omega)$, with $\ell \geq 1, p = m+1$, given in (2.2) and further define

$$\boldsymbol{\mathcal{V}}_{0,D} := \{\boldsymbol{\phi} \in \boldsymbol{\mathcal{V}} : \operatorname{div}\boldsymbol{\phi} = 0,\ \boldsymbol{\phi} = 0\, on\, \Gamma_D\}. \tag{2.22}$$

Using these notations, we can write the equilibrium of Ω at a time t as,

$$\int_\Omega \boldsymbol{s}(\mathbf{v}) : \dot{\boldsymbol{\varepsilon}}(\boldsymbol{\phi})\,dx - \int_\Omega P\mathbf{I} : \dot{\boldsymbol{\varepsilon}}(\boldsymbol{\phi})\,dx - \int_{\Gamma_N} \boldsymbol{T}\cdot\mathbf{v}\,dS = \int_\Omega \mathbf{f}\cdot\boldsymbol{\phi}\,dx, \quad \forall\boldsymbol{\phi} \in \boldsymbol{\mathcal{V}}_{0,D}. \tag{2.23}$$

We neglect the volume forces, e.g., the inertia and the gravity forces, and set $\mathbf{f} = 0$. Now, we consider the hydrostatic pressure P as the Lagrange multiplier for enforcing the constraint

$\mathrm{div}(\mathbf{v}) = 0$, and set the following saddle point problem: find the velocity $\mathbf{v} \in \boldsymbol{\mathcal{V}}_D := \{\boldsymbol{\phi} \in \boldsymbol{\mathcal{V}} : \boldsymbol{\phi} = 0 \, on \, \Gamma_D\}$ and the pressure $P \in L^q(\Omega)$ with $q = \frac{p}{p-1}$ such that

$$\begin{cases} \int_\Omega \boldsymbol{s}(\mathbf{v}) : \dot{\boldsymbol{\varepsilon}}(\boldsymbol{\phi})\, dx - \int_\Omega P\boldsymbol{I} : \dot{\boldsymbol{\varepsilon}}(\boldsymbol{\phi})\, dx - \int_{\Gamma_N} \boldsymbol{T} \cdot \boldsymbol{\phi}\, dS & = 0, \\ \int_\Omega \mathrm{div}(\mathbf{v})\, Q\, dx & = 0, \end{cases} \tag{2.24}$$

for all $\boldsymbol{\phi} \in \boldsymbol{\mathcal{V}}$ and $Q \in L^q(\Omega)$. We emphasize that the unknown $\mathbf{v}$ appears implicitly in (2.24) by means of the tensor $\mathbf{s}$, which is a function of the strain rate tensor $\dot{\boldsymbol{\varepsilon}}$, which in turn is a function of $\mathbf{v}$. The pressure P is a Lagrange multiplier for the incompressibility condition $\mathrm{div}(\mathbf{v}) = 0$.

2.6 Contact between two bodies

Following the above formulation, we consider the friction contact problem between two viscoplastic bodies, which can undergo a finite deformation. The two bodies in their initial (reference) configuration are given by Ω_1 and Ω_2 with $\Omega_i \subset \mathbb{R}^2$, $i = 1, 2$. The associated boundaries $\partial\Omega_i$ are divided into three disjoint parts: (i) $\Gamma_D^{(i)}$, where the displacements are prescribed, (ii) $\Gamma_N^{(i)}$, where the stresses are prescribed, and (iii) the common contact part Γ_C, where contact conditions will be defined. We assume $\mid \Gamma_D^{(i)} \mid > 0$ for $i = 1, 2$. On Γ_C, we define the normal vector $\mathbf{n}_{12}$ in the direction towards the interior of Ω_2. We use the subindex $i = 1$ or $i = 2$ to denote the restriction on the associated domains Ω_1 or Ω_2 respectively. The stress vectors on Γ_C are given by

$$\mathbf{T}_1 = \boldsymbol{\sigma}_1 \cdot \mathbf{n}_{12}, \quad \mathbf{T}_2 = \boldsymbol{\sigma}_2 \cdot (-\mathbf{n}_{12}). \tag{2.25}$$

Both stresses act on the contact area Γ_c and are opposite by obeying the principle of action and reaction, i.e., $\mathbf{T_1} = \boldsymbol{\sigma}_1 \cdot \mathbf{n}_{12} = -\boldsymbol{\sigma_2} \cdot \mathbf{n}_{21} = -\mathbf{T_2}$. Each of the stress vectors $\mathbf{T}_i$, $i = 1, 2$ can be decomposed with respect to $\mathbf{n}_{12}$ into a normal $\mathbf{T}_{i,n}$ and a tangential component $\boldsymbol{T}_{i,\tau}$, [32], for example for $i = 1$

$$\mathbf{T}_{1,n} = (\boldsymbol{T}_1 \cdot \mathbf{n}_{12})\mathbf{n}_{12}, \quad \mathbf{T}_{1,\tau} = \mathbf{T}_1 - (\boldsymbol{T}_1 \cdot \mathbf{n}_{12})\mathbf{n}_{12}. \tag{2.26}$$

The scalar $\sigma_n := \sigma_n^1 = \boldsymbol{T}_1 \cdot \mathbf{n}_{12} < 0$ (in compression) is the normal stress, and the tangential vector $\boldsymbol{T}_{i,\tau}$ (orthogonal to $\mathbf{n}_{12}$) is associated with the friction forces on Γ_C, [32]. On the interface Γ_C, we define the velocity difference $\Delta\mathbf{v} = \mathbf{v}_1 - \mathbf{v}_2$ and the relative slip velocity

$$\mathbf{v}_s = \Delta\mathbf{v} - (\Delta\mathbf{v} \cdot \mathbf{n}_{12})\mathbf{n}_{12}. \tag{2.27}$$

Along the contact interface Γ_C the bodies can not interpenetrate, i.e., $\Omega_1 \cap \Omega_2 = \emptyset$. The continued bilateral contact between Ω_1 and Ω_2 without penetration is usually expressed by $\Delta\mathbf{v} \cdot \mathbf{n}_{12} = 0$. In view of this, during the numerical computations, we have to take into account the conditions

$$g_n := \Delta\mathbf{v} \cdot \mathbf{n}_{12} = 0, \tag{2.28a}$$

$$\sigma_n < 0, \tag{2.28b}$$

across the contact area Γ_C. Several methods have been presented in the literature for incorporating the contact constraints (2.28) in the variational form and in the finite element discrete analogue, see, e.g., [21], [32], and the references therein. Here, we will apply the penalty method, where an extra term is introduced to penalize the velocity of having a normal penetration component.

Remark 2.5. Note that for the two normal stresses $\sigma_n^1 = \boldsymbol{T}_1 \cdot \mathbf{n}_{12} = -(\boldsymbol{\sigma}_2 \cdot \mathbf{n}_{21}) \cdot \mathbf{n}_{12} = (\boldsymbol{\sigma}_2 \cdot \mathbf{n}_{21}) \cdot \mathbf{n}_{21} = \sigma_n^2$ holds. By this condition we can also infer that $\sigma_n^1 = \sigma_n^2$, which indicates that the normal interface stresses are compressive, and so this requires $\sigma_n^1 < 0$, compare with (2.28b).

Remark 2.6. The sticking (frictionless) contact conditions are $\Delta\mathbf{v} = 0$ and $(\boldsymbol{\sigma}_2 \cdot \mathbf{n}_{21}) + (\boldsymbol{\sigma}_1 \cdot \mathbf{n}_{12}) = 0$.

Frictional contact In general, for deriving a relation which can describe in an complete way the interfacial friction phenomena and the friction tangential stresses $\mathbf{T}_\tau$, apart from the normal stress and the relative tangential velocity, one must also take into account some other physical parameters, such as temperature, surface roughness, interaction of chemical processes, etc, which are often described in micro-scales. It is clear that the mixing and the interrelation of all these quantities will lead to a complicated model. In simple practical applications the classical Coulomb's law, which includes the normal stress and the relative velocity, or Tresca's law, which includes a constant shear strength, are usually used, [20], [5], [32], [2]. For the purposes of this work, we introduce a nonlinear friction law that is compatible with (2.20) (without threshold), which describes the tangential effects and can be considered as a generalization of Tresca's law. Accordingly we let

$$\mathbf{T}_\tau = -a_f K |\mathbf{v}_s|^{m-1}\mathbf{v}_s, \tag{2.29a}$$

where a_f is a friction parameter, which is estimated below, and K is a material parameter which can be dependent on stain hardening, see (2.15). In this case the interface conditions are completed by adding the bilateral contact condition (2.28a).

3 Application to strip rolling

As we mentioned in the previous sections, the hot strip rolling process is very important and most commonly used technique in engineering metal-forming, since it is used for the design of rotating machine parts, gears, ball bearings, etc, [10], [8], [15], [18], [33]. In the flat rolling process the thickness of a flat metal plate (strip) is reduced by passing it between two counter-rotating cylinders (rollers) which have a fixed distance, as shown in an illustration in Fig. 1(a). For an analysis of rolling problems we refer to [16], [15], [33]. We use the relations and the forms that were derived in the previous section for describing the rolling process. In our study the metal plate is the viscoplastic material that occupies Ω_1 and the rollers are the rigid tools Ω_2. We take advantage of the X-axis symmetry of the problem and consider the upper half of the problem, see Fig. 1(a). We focus on deriving the problem formulation for the case of having maximum length of the contact interface Γ_C, and setting symmetry boundary conditions along the X-axis. A schematic illustration of the boundary parts of $\partial\Omega_1$ with the associated boundary conditions is given in Fig. 1(b). Since all the quantities below are related to the deformation of the plate, i.e., Ω_1, we remove the corresponding index from their notation.

3.1 The boundary value problem for the rolling contact

During the rolling process, the metal plate is moving between the two rollers and the tangential friction forces that exist across the interface Γ_C drive the plate in to the gap. At the inlet points, i.e., points on the left vertical boundary Γ_{in}, see Fig. 1(b), the velocity of the plate $\mathbf{v}_{in}$ is lower than the tangential velocity of the rollers. As the plate moves in to the gap of the rollers, it is compressed and this increases its velocity due to the conservation of mass. At the neutral point, $P_{neutral}$ on Γ_C, the relative velocity is $\mathbf{v}_s = 0$ and finally the plate exits the roller gap with velocity $\mathbf{v}_{out}$, which is greater than the velocity of the rollers, see Fig. 1(b). Since additional elastic phenomena are ignored, these remarks lead to the following constraints on the boundary

$$\mathbf{v}\cdot(-\mathbf{n}_{in}) \leq |\mathbf{U}_{roll,\tau}| \text{ on } \Gamma_{in} \quad \text{and} \quad \mathbf{v}\cdot(\mathbf{n}_{out}) \geq |\mathbf{U}_{roll,\tau}| \text{ on } \Gamma_{out}, \tag{3.1}$$

where $|\mathbf{U}|_{roll,\tau}$ is the measure of the tangential velocity of the roller. We apply penalty method techniques, [11], [9], for treating the boundary constraints given in (3.1), the bilateral contact constraint in (2.28a) and the constraint for preventing the vertical motion on the free-stress boundary parts denoted by Γ_0 in Fig. 1(b). For a function $f : \bar{\Omega}_1 \cup \bar{\Omega}_2 \to \mathbb{R}$ we define $\big[f(x)\big]_+ := \max\{f(x), 0\}$ and introduce the penalty functionals

$$\Psi_{in}(\mathbf{v}) = \frac{\gamma_{in}}{2} \int_{\Gamma_{in}\cup\Gamma_{0L}} \Big(\big[\mathbf{v}\cdot(-\mathbf{n}_{in}) - |\mathbf{U}_{roll,\tau}|\big]_+\Big)^2\, ds, \tag{3.2a}$$

$$\Psi_{out}(\mathbf{v}) = \frac{\gamma_{out}}{2} \int_{\Gamma_{out}\cup\Gamma_{0R}} \Big(\big[-\mathbf{v}\cdot(\mathbf{n}_{out}) + |\mathbf{U}_{roll,\tau}|\big]_+\Big)^2\, ds, \tag{3.2b}$$

$$\Psi_{vC}(\mathbf{v}) = \frac{\gamma_{vC}}{2} \int_{\Gamma_C} \Big(\big[|\Delta\mathbf{v}\cdot\mathbf{n}_C|^2 - Tol\big]_+\Big)^2\, ds, \tag{3.2c}$$

$$\Psi_{\Gamma_0}(\mathbf{v}) = \frac{\gamma_{v0}}{2} \int_{\Gamma_0} \big(\mathbf{v}\cdot\mathbf{n}_{\Gamma_0}\big)^2\, ds, \tag{3.2d}$$

where γ_{in}, γ_{out}, γ_{vC} and γ_{v0} are the penalty parameters (their values will be specified later), $\mathbf{n}_{in}$, $\mathbf{n}_{out}$, $\mathbf{n}_C$ and $\mathbf{n}_{\Gamma_0}$ are the normals on the associated boundary parts, and the tolerance $Tol \approx 1.E-05$. In (3.2) the boundary parts Γ_{0L} and Γ_{0R} are the free-stress boundary parts with points (x, y) such that $\Gamma_{0L} := \{(x, y) \in \Gamma_0 : x \le x_{neutral\,point}\}$ and $\Gamma_{0R} := \{(x, y) \in \Gamma_0 : x \ge x_{neutral\,point}\}$. Thus, utilizing (2.24), (2.29a) and (3.2) we can express the following penalty formulation for the rolling problem: find $\mathbf{v}$ and P such that

$$\begin{cases} \displaystyle\int_{\Omega_1} \boldsymbol{s}(\mathbf{v}) : \dot{\boldsymbol{\varepsilon}}(\boldsymbol{\phi})\, dx - \int_{\Omega_1} P\boldsymbol{I} : \dot{\boldsymbol{\varepsilon}}(\boldsymbol{\phi})\, dx - \int_{\Gamma_0\cup\Gamma_{in}} \boldsymbol{T}_0\cdot\boldsymbol{\phi}\, dS - \int_{\Gamma_C} \boldsymbol{T}_\tau\cdot\boldsymbol{\phi}\, dS + \int_{\Gamma_{out}} \mathbf{T}^*\cdot\boldsymbol{\phi}\, dS \\ \displaystyle -\gamma_{in} \int_{\Gamma_{in}\cup\Gamma_{0L}} \big[\mathbf{v}\cdot(-\mathbf{n}_{in}) - |\mathbf{U}_{roll,\tau}|\big]_+ \boldsymbol{\phi}\cdot\mathbf{n}_{in}\, dS - \gamma_{out} \int_{\Gamma_{out}\cup\Gamma_{0R}} \big[-\mathbf{v}\cdot(\mathbf{n}_{out}) + |\mathbf{U}_{roll,\tau}|\big]_+ \boldsymbol{\phi}\cdot\mathbf{n}_{out}\, dS \\ \displaystyle -\gamma_{v0} \int_{\Gamma_0} \big(\mathbf{v}\cdot\mathbf{n}_{\Gamma_0}\big)\boldsymbol{\phi}\cdot\mathbf{n}_{\Gamma_0}\, dS - \gamma_{vC} \int_{\Gamma_C} \big[|\Delta\mathbf{v}\cdot\mathbf{n}_C|^2 - Tol\big]_+ \boldsymbol{\phi}\cdot\mathbf{n}_C\, dS = 0, \\ \displaystyle\int_\Omega \mathrm{div}(\mathbf{v})\, Q\, dx = 0, \end{cases} \tag{3.3}$$

for all test functions $\boldsymbol{\phi} \in \boldsymbol{\mathcal{V}}$ and $Q \in L^q(\Omega)$ where $\Gamma_0 \cup \Gamma_{in}$ are the free stress boundary parts, i.e., $\mathbf{T}_0 = 0$, and $\mathbf{T}^*$ on Γ_{out} describes the free stress condition plus a penalty correction term that prevents the points $\mathbf{x} \in \Gamma_{out}$ to move vertically (along Y-axis) to the main movement of the plate along X-axis.

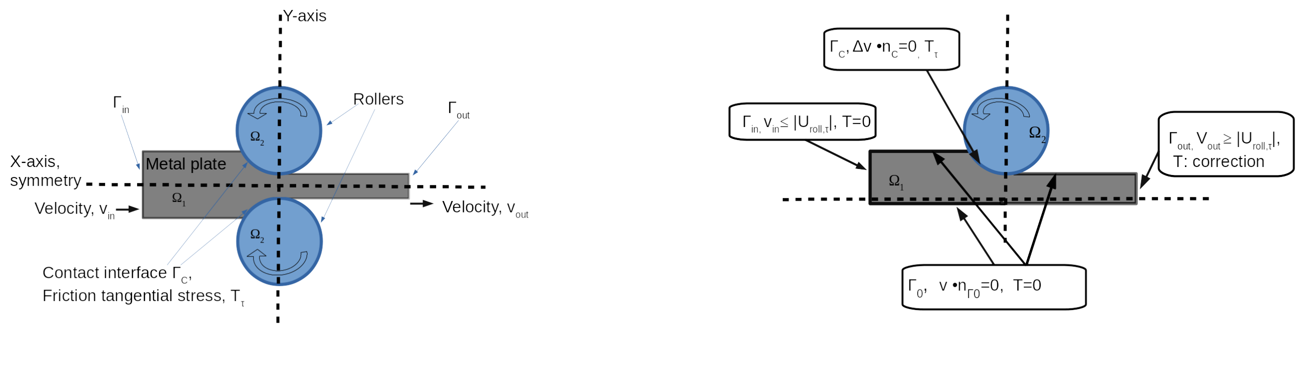

(a) (b)

Fig. 1. Schematic diagram of the rolling problem, (a) the rollers with the deformed plate and the $X - axis$ symmetry line, (b) the boundary parts on $\partial\Omega_1$ with the associated boundary conditions.

3.2 Finite element discretization

We use finite element methodology to discretize (3.3). Each domain Ω_i, $i = 1, 2$ is subdivided into a collection T_h^i of (conforming) triangular mesh elements $\{K\}$ such that $\Omega_i = \cup_{K \in T_h^i} K$. We set $T_h = T_h^1 \cup T_h^2$. We define the mesh size $h_i\, i = 1, 2$ to be the length of the maximum edge of $K \in T_h^i$. On each T_h^i we consider the space $V_{h,k}^i$ of continuous piece-wise polynomials of order κ, i.e,

$$V_{h,\kappa}^i = \{v_h : v_h \in C^0(\Omega_i), v_h|_K \in \mathbb{P}^\kappa(K), K \in T_h^i\}, \tag{3.4}$$

where C^0 is the space of continuous functions and $\mathbb{P}^\kappa$ is the space of polynomials of order κ. Let $\{\phi_j^i\}_{j=1}^{N_i}$, $i = 1, 2$ be a corresponding basis of each $V_{h,\kappa}^i$, which is defined through the N_i nodes of T_h^i. Then, for every $v_h \in V_{h,\kappa}^i$ we have

$$v_h = \sum_{j=1}^{N_i} a_j \phi_j^i(x, y), \tag{3.5}$$

where a_i are the related N_i nodal values of v_h, see details in [14], [3]. In view of (3.4) the discrete analogue of (3.3) is: find $\mathbf{v}_h := (v_{1,h}, v_{2,h}) \in V_{h,\kappa}^1 \times V_{h,\kappa}^1$ and $P_h \in V_{h,l}^1$ such that

$$\begin{cases} \displaystyle\int_{\Omega_1} \boldsymbol{s}(\mathbf{v}_h) : \dot{\boldsymbol{\varepsilon}}(\boldsymbol{\phi}_h)\, dx - \int_{\Omega_1} P_h \boldsymbol{I} : \dot{\boldsymbol{\varepsilon}}(\boldsymbol{\phi}_h)\, dx - \int_{\Gamma_C} \boldsymbol{T}_{\tau,h} \cdot \boldsymbol{\phi}_h\, dS + \int_{\Gamma_{out}} \mathbf{T}_{0,h}^* \cdot \boldsymbol{\phi}_h\, dS & \\ \displaystyle -\gamma_{in} \int_{\Gamma_{in} \cup \Gamma_{0L}} \big[\mathbf{v}_h \cdot (-\mathbf{n}_{in}) - |\mathbf{U}_{roll,\tau}|\big]_+ \boldsymbol{\phi}_h \cdot \mathbf{n}_{in}\, dS & \\ \displaystyle -\gamma_{out} \int_{\Gamma_{out} \cup \Gamma_{0R}} \big[- \mathbf{v}_h \cdot (\mathbf{n}_{out}) + |\mathbf{U}_{roll,\tau}|\big]_+ \boldsymbol{\phi}_h \cdot \mathbf{n}_{out}\, dS & \\ \displaystyle -\gamma_{v_0} \int_{\Gamma_0} \big(\mathbf{v}_h \cdot \mathbf{n}_{\Gamma_0}\big) \boldsymbol{\phi}_h \cdot \mathbf{n}_{\Gamma_0}\, dS - \gamma_{v_C} \int_{\Gamma_C} \big[|\Delta \mathbf{v}_h \cdot \mathbf{n}_C|^2 - Tol\big]_+ \boldsymbol{\phi}_h \cdot \mathbf{n}_C\, dS & = 0, \\ \displaystyle\int_{\Omega} \operatorname{div}(\mathbf{v}_h)\, Q_h\, dx & = 0, \end{cases} \tag{3.6}$$

for $\boldsymbol{\phi}_h := (\phi_{1,h}, \phi_{2,h}) \in V_{h,\kappa}^1 \times V_{h,\kappa}^1$ and $Q_h \in V_{h,l}^1$.

Note that different meshing of the contact Γ_C can occur through the nodes on $\partial\Omega_i$. We can have matching mesh nodes and non-matching mesh nodes. For producing the finite element solutions, we need to first identify the nodes that lay on the contact interface, and the rest nodes which are located away from the contact area. In the most realistic cases with finite deformations, we prefer to perform the computations without requiring matching mesh restrictions across Γ_C. We note here that the tangential velocities of the two bodies are not equal, and the domain Ω_2 (roller) has a fixed known tangential velocity. Due to the frictional shear stresses (2.29a), the variation of the relative interface velocity $\mathbf{v}_s$ and the conditions in (3.1), the mesh nodes enter and leave Γ_C with different rates. The non-penetration of the bodies on γ_C is enforced in the numerical computations through the penalty terms related to (2.28a). In (3.6) the spaces $V_{h,\kappa}^1$ and $V_{h,l}^1$ has been chosen to satisfy the in-sup condition, i.e., in our numerical examples we set $l = k - 1$, [28]. The configuration is updated following an explicit procedure, (see Section 3.3 below).

3.3 Explicit time integration

As the material passes through the gap of the rollers the rolling becomes a steady state process. We find numerically the steady-state solution by using an explicit time-stepping algorithm for updating the configuration. The whole time period of the study of the problem, let say $T = [0, T_F]$, is partitioned into small time increments $[t_n, t_{n+1}]$, $t_{n+1} = t_n + \Delta t$ with fixed time step Δt. In a sequential repeating procedure, we solve (3.6) at time t_n and then using the computed velocity $\mathbf{v}_{h,t_n}$ we find (approximately) the new configuration $\Omega_{t_{n+1}}$ at t_{n+1} by updating the coordinates $\mathbf{x}^{node}$ of the mesh nodes

$$\mathbf{x}_{t_{n+1}}^{node} = \mathbf{x}_{t_n}^{node} + \Delta t \mathbf{v}_{h,t_n}. \tag{3.7}$$

In (3.7) $\mathbf{x}_{t_{n+1}}^{node}$ are the new coordinates of the mesh nodes of $\Omega_{t_{n+1}}$ which is going to be used as the new reference configuration. The computations are being repeated for the next configurations following the procedure described previously. We solve (3.6) on $\Omega_{t_{n+1}}$ and applying (3.7) compute the coordinates of the mesh notes of $\Omega_{t_{n+2}}$.

3.4 Implementation remarks

The final nonlinear algebraic system resulting from (3.6) is solved by using a simple Picard iterative method of the type

$$\begin{aligned}
&\text{for every time step } t_n,\ n = 1, 2, \ldots \text{ solve} && (3.8a)\\
&\mathbf{J}(\mathbf{U}_n^i)\mathbf{U}_n^{i+1} = \mathbf{b}(\mathbf{U}_n^i, \mathbf{U}_{roll}), \quad \text{for} \quad i = 0, 1, \ldots, i_{max}, && (3.8b)\\
&\text{when } \ \|\mathbf{U}_n^i - \mathbf{U}_n^{i+1}\| \leq 1.E-05 \quad \text{set } \mathbf{U}_n^{i+1} := \mathbf{U}_n^{solution}, && (3.8c)\\
&\text{and move to the next time step,} && (3.8d)
\end{aligned}$$

where for every interior iteration i the vector $\mathbf{U}_n^i$ includes the unknown degrees of freedom of $\mathbf{v}_h$ and P_h, $\mathbf{J}$ is the linearized matrix which includes the non-linearities of (2.21) and (2.29a) computed using the previous iteration $\mathbf{U}_n^i$, $\mathbf{b}$ is the right hand side and $\mathbf{U}_n^{solution}$ is the final solution for the time step t_n. In the numerical tests we have set $i_{max} = 20$, but as we approach the steady-state the criterion in (3.8c) is satisfied in less than 10 iterations.

The value for the small constant ε_0 in (2.21) is set to 1.E-04. In order to avoid a singular behavior of the stress form (2.21), we solve the associated linear system in (3.6), by setting $m = 1$, during the first iteration $i = 0$ at the first time step t_1, and then we use the corresponding solutions to compute the entries of $\mathbf{J}(\mathbf{U}_1^{i=1})$ in (3.8b). The solution of the linear system provides an initial guess for the velocity which is corrected during the next iterative steps of the scheme given in (3.8).

Within the application of the finite element scheme (3.6) at every time increment, it is necessary to know which nodes are in contact and which are on free stress boundary parts at every time step. Having known the mesh nodes which are on Γ_C at t_n we need to find the points which are in contact at the end of the time increment, i.e., after computing the new configuration using (3.7). In fact this is mainly related to the position of the upper boundary points which enter or leave from the contact zone. We suppose that the points which are or which are not on Γ_C remain in the same state throughout the interior steps of the iterative procedure (3.8). The control for changing the boundary characterization of the upper part of the boundary points is performed after the node update obtained from (3.7). Due to the small variations of $\Delta \mathbf{v}_s \cdot \mathbf{n}_C$ at the entrance/exit contact points, we prefer to apply the geometric condition

$$\begin{aligned}
&\text{if} \quad \|\mathbf{x}_{t_{n+1}}^{node} - \Pi(\mathbf{x}_{t_{n+1}}^{node})\| < 1.E-05, \text{then} \quad \mathbf{x}_{t_{n+1}}^{node} \in \Gamma_C, && (3.9a)\\
&\text{if} \quad \|\mathbf{x}_{t_{n+1}}^{node} - \Pi(\mathbf{x}_{t_{n+1}}^{node})\| \geq 1.E-05, \text{then} \quad \mathbf{x}_{t_{n+1}}^{node} \quad \text{is a free stress point,} && (3.9b)
\end{aligned}$$

where $\Pi(\mathbf{x}_{t_{n+1}}^{node})$ is the orthogonal projection of $\mathbf{x}_{t_{n+1}}^{node}$ to the roll surface.

The interface Γ_C is approximated by linear elements and through this approximation large overlap and/or gap regions can exist between the mesh points of the plate and the roller surface (specially for coarse mesh tests). In order to avoid the existence of these large overlap/gap regions, every ten time steps we apply a post-processing correction for the locations of the internal mesh nodes of $\varGamma_C$, i. e., we correct the position of the nodes based on maximum distance function given in (3.9a).

Due to the change in the boundary conditions on the last contact point $M = (1, 0.2)$ the normal pressure can exhibit an oscillatory behavior. A post-processing correction is applied on the elements after the last exit contact point in order to eliminate the oscillations of the normal pressure.

The maximum distance function given in (3.9a) helps in defining the time step $\varDelta t$. In our computations we have chosen $\varDelta t = \frac{h_C}{6}$, where h_C is the mesh size across $\varGamma_C$.

As the plate is driven out of the roller gap, the penalty functionals given in (3.2) are applied for all the corresponding boundary parts of $\partial\varOmega_1$ which are formed after the rolling, see Fig. 1(b) and Fig. 2(b). Since the neutral point $P_{neutral}$ has no fixed location until reaches to the steady-state, in our computations we specify $\varGamma_{0L}$ and $\varGamma_{0R}$ with respect to the last contact point $M = (1, 0.2)$, i. e., $\varGamma_{0L} := \{(x, y) \in \varGamma_0 : x \leq 1\}$ and $\varGamma_{0R} := \{(x, y) \in \varGamma_0 : x \geq 1\}$.

The values of the parameters in (3.2) are given in the following Table 1

	$I = [0.75, 0.775]$			
parameter	$x \in I$	$x \notin I$	$\varGamma_{in}$	$\varGamma_{out}$
γ_{v_0}	$\frac{10}{h}$	$\frac{25}{h}$	-	-
γ_{v_C}	$\frac{10}{h}$	$\frac{25}{h}$	-	-
$\gamma_{v_{in}}$	-	-	$\frac{2}{h^{m+1}}$	-
$\gamma_{v_{out}}$	-	-	-	$\frac{2}{h^{m+1}}$

Table 1. The values of the penalty parameters.

3.5 Stability bounds and an estimation of a_f

The value of the friction parameter a_f in (2.29a) is in general unknown. Below we try to give an estimate for a_f by providing stability bounds for the scheme (3.6). Consider (3.6) without the introduction of the boundary constraints and free stress $\mathbf{T} = 0$. We set $m - 1 = p - 2$, with $p > 1$. Setting $\boldsymbol{\phi}_h = \mathbf{v}_h$ and $Q_h = P_h$ in variational formulation (3.6), and recalling that $\boldsymbol{s} = 2K(\sqrt{3}\dot{\varepsilon}_{eq})^{m-1}\dot{\boldsymbol{\varepsilon}}$ and $\mathbf{T}_\tau = -a_f K|\mathbf{v}_s|^{m-1}\mathbf{v}_s$, we can obtain

$$\int_{\varOmega_1} 2K(\sqrt{3}\dot{\varepsilon}_{eq})^{p-2}\dot{\boldsymbol{\varepsilon}} : \dot{\boldsymbol{\varepsilon}}\, dx + \int_{\varGamma_C} a_f\, |\mathbf{v}_{h,s}|^{p-2}\mathbf{v}_{h,s} \cdot \mathbf{v}_h\, ds = 0. \tag{3.10}$$

Using the decomposition $\mathbf{v}_h = \mathbf{v}_{h,\tau} + \mathbf{v}_{h,n}$ with $\mathbf{v}_{h,\tau} \cdot \mathbf{v}_{h,n} = 0$ in (3.10) we get

$$\begin{aligned}
\int_{\varOmega_1} C_K(\dot{\varepsilon}_{eq})^p\, dx &= -\int_{\varGamma_C} a_f\, |\mathbf{v}_{h,s}|^{p-2}\mathbf{v}_{h,s} \cdot (\mathbf{v}_{h,\tau} + \mathbf{v}_{h,n} - \mathbf{U}_{roll,\tau} + \mathbf{U}_{roll,\tau})\, ds \\
&= -\int_{\varGamma_C} a_f\, |\mathbf{v}_{h,s}|^{p-2}\mathbf{v}_{h,s} \cdot (\mathbf{v}_{h,s} + \mathbf{v}_{h,n} + \mathbf{U}_{roll,\tau})\, ds \\
&= -\Big(\int_{\varGamma_C} a_f\, |\mathbf{v}_{h,s}|^p\, ds + \int_{\varGamma_C} a_f\, |\mathbf{v}_{h,s}|^{p-2}\mathbf{v}_{h,s} \cdot (\mathbf{v}_{h,n} + \mathbf{U}_{roll,\tau})\, ds\Big) \\
&= -\int_{\varGamma_C} a_f\, |\mathbf{v}_{h,s}|^p\, ds + \int_{\varGamma_C^-} a_f\, |\mathbf{v}_{h,s}|^{p-1}|\mathbf{U}_{roll,\tau}|\, ds - \int_{\varGamma_C^+} a_f\, |\mathbf{v}_{h,s}|^{p-1}|\mathbf{U}_{roll,\tau}|\, ds, \\
&= -\int_{\varGamma_C} a_f\, |\mathbf{v}_{h,s}|^p\, ds + \int_{\varGamma_C} a_f\, |\mathbf{v}_{h,s}|^{p-1}|\mathbf{U}_{roll,\tau}|\, ds - 2\int_{\varGamma_C^+} a_f\, |\mathbf{v}_{h,s}|^{p-1}|\mathbf{U}_{roll,\tau}|\, ds,
\end{aligned} \tag{3.11}$$

where we used that $\mathbf{v}_{h,s}$ and $\mathbf{U}_{roll,\tau}$ are parallel, and defined $\varGamma_C^+ := \{(x, y) \in \varGamma_C : \mathbf{v}_{h,s} \cdot \mathbf{U}_{roll,\tau} = |\mathbf{v}_{h,s}|\, |\mathbf{U}_{roll,\tau}|\}$ and analogously $\varGamma_C^- := \{(x, y) \in \varGamma_C : \mathbf{v}_{h,s} \cdot \mathbf{U}_{roll,\tau} = -|\mathbf{v}_{h,s}|\, |\mathbf{U}_{roll,\tau}|\}$. Note that since $\mathbf{v}_{h,s}$ and $\mathbf{U}_{roll,\tau}$ are parallel there exists a $\lambda : \lambda(x)$, $|\lambda| < 1$ such that $\mathbf{v}_{h,s} = \lambda \mathbf{U}_{roll,\tau}$. Furthermore note that on Γ_C^- it holds that $|\mathbf{v}_{h,\tau}| < |\mathbf{U}_{roll,\tau}|$. On the other hand the difference $\mathbf{v}_{h,\tau} - \mathbf{U}_{roll,\tau}$ across Γ_C^+ is very small, and since $p-1>0$, we then may suppose

$$|\mathbf{v}_{h,s}|^{p-1} \approx 0 \quad \text{on} \quad \Gamma_C^+. \tag{3.12}$$

Now, in (3.11) we apply inequalities (2.3) with $p-1 = \frac{p}{q}$, and find

$$\begin{aligned} \int_{\Omega_1} C_K(\dot{\varepsilon}_{eq})^p \, dx \geq & \int_{\Gamma_C} a_f \left(|\lambda|^{p-1}| - |\lambda|^p|\right) \mathbf{U}_{roll,\tau}|^p \, ds \\ & - c_{1,\epsilon} \int_{\Gamma_C^+} |\mathbf{v}_{h,s}|^p \, ds - c_{2,\epsilon} \int_{\Gamma_C^+} a_f^p \, |\mathbf{U}_{roll,\tau}|^p \, ds. \end{aligned} \tag{3.13}$$

Finally, we select the parameter $c_{2,\epsilon}$ in (3.13) sufficiently small, e. g., $c_{2,\epsilon} = \frac{1}{2a^{p-1}} \min\{|\lambda|^{p-1}| - |\lambda|^p\}$ and obtain

$$\int_{\Omega_1} C_K(\dot{\varepsilon}_{eq})^p \, dx + c_{1,\epsilon} \int_{\Gamma_C^+} |\mathbf{v}_{h,s}|^p \, ds \geq \int_{\Gamma_C} \frac{a_f}{2} \min\{|\lambda|^{p-1}| - |\lambda|^p\} |\mathbf{U}_{roll,\tau}|^p \, ds. \tag{3.14}$$

The lower bound given in (3.14) seems not so convenient for estimating the parameter a_f. In view of (3.12) we can consider that the corresponding integrals on Γ_C^+ have negligible contribution to the right hand side in (3.11). Thus based on that we omit these integrals through our computations and using further the inequalities [3], $\sum_K \|\nabla \mathbf{v}_h\|_{L^p(K)} \leq \frac{C}{h} \sum_K \|\mathbf{v}_h\|_{L^p(K)}$ for $\mathbf{v}_h \in V_{h,\kappa}^1 \times V_{h,\kappa}^1$, and $(|a|^2 + |b|^2)^{\frac{p}{2}} \leq 2^{p-1}(|a|^p + |b|^p)$, we deduce that

$$\frac{C_5}{h} \sum_K \int_K |\mathbf{v}_h|^p \, dx \geq \int_{\Gamma_{C-}} a_f \, \min\{|\lambda|^{p-1}| - |\lambda|^p\} |\mathbf{U}_{roll,\tau}|^p \, ds \tag{3.15}$$

Owing that $|\mathbf{U}_{roll,\tau}|$ is fixed, the magnitude of $\min\{|\lambda|^{p-1}| - |\lambda|^p\}$ can be estimated from the values of $|\mathbf{v}_{h,\tau}|$ and $|\mathbf{U}_{roll,\tau}|$ on the first touching mesh element in the gap entry. Note again that we accept that $\mathbf{v}_{h,\tau}$ and $\mathbf{U}_{roll,\tau}$ are parallel across the touching element.

Remark 3.1. The relations (3.13) and (3.14) hold also for the continuous solution $\mathbf{v}$ of (3.3).

Remark 3.2. The relation (3.15) provides an estimation of a_f by means of the discrete kinematic energy and the measure $|\mathbf{U}_{roll,\tau}|^p$.

Remark 3.3. In the numerical examples we estimate a_f by (3.15), where the integrals $\int_K |\mathbf{v}_h|^p \, dx$ are computed numerically using the values $\mathbf{U}_n^i$ of the previous iteration, see (3.8), and setting $C_5 = 2^p$.

Remark 3.4. Applying similar computations as above and using (2.3) we can obtain the upper bound

$$\int_{\Omega_1} C_K(\dot{\varepsilon}_{eq})^p \, dx + c_{1,\varepsilon} \int_{\Gamma_C} a_f \, |\mathbf{v}_{h,s}|^p \leq c_{2,\varepsilon} \int_{\Gamma_C} a_f \, |\mathbf{U}_{roll,\tau}|^p \, ds. \tag{3.16}$$

4 Numerical examples

In this section, we perform numerical examples for the steady state rolling problem. Note that due to the symmetry of the problem with respect to $X-$axis, we consider only the upper half of the problem. The radius of the roll is $R = 0.6m$ and the center is the point $C_{roll} := (X_{roll}, Y_{roll}) = (1, 0.8)$. The initial length of the metal plate is $L = 4m$ ($-3 \leq x \leq 1$) and the maximum height $H = 0.25m$ $(0 \leq y \leq 0.25)$, respectively. The contact interface consists of the points $\Gamma_C = \{(x, y) : 0.760208428 \leq x \leq 1,\ 0.2 \leq y \leq 0.25,\ \text{and}\ \left((x - X_{Roll})^2 + (y - Y_{roll})^2\right)^{\frac{1}{2}} = 0.6\}$. Therefore, the thickens of the plate at the entrance is $0.25m$ and at the exit is $0.2m$. An illustration of the initial configuration of the problem with the touching zone and uniform mesh for the plate are shown in Fig. 2(a). In order to examine the convergence of the numerical solution and the mesh-independency, the problem is solved using four different uniform meshes. The corresponding mesh sizes with the associated abbreviations are listed in Table 2. The meshes are separated into three groups: $C1$ and $C2$ are the coarse meshes, $M1$ and $M2$ are the middle meshes, while $F1$ and $F2$ are the fine meshes. The mesh size refers to the mesh size of the boundary elements, say h, that are in contact with the interface of the initial configuration. For every mesh-test case, we start the computation having a maximum length of contact, Fig. 2(a), and use a fixed time step $\Delta t = \frac{h}{6}$.

During the first initial computations we set $m = 0.2$ and the angular velocity for the roller, i. e., the rate of change of angle with respect to time, is $\theta = \frac{\pi}{3}$ per second. In the last examples we solve the problem using $m \in \{0.15, 0.25\}$ and $\theta = \frac{\pi}{6}$, and compare the associated numerical results.

The evolution of the deformation is depicted in Fig. 2. The results have been computed using the $C2$ mesh, see Table 2. Fig. 2(b) shows the deformed (after the rolling) and the undeformed (before the rolling) parts of the plate at the half computational time. In Fig. 2(c) the velocity vectors with the associated mesh in the contact region are plotted, from which, the sharp variation of the velocity near the first touching mesh element of the roller entry can be seen. Fig. 2(d) shows the deformed plate with the distribution of the magnitude of the stress-rate $\sigma_{ef} = K 3^{\frac{m+1}{2}} \dot{\varepsilon}_{vp}^{m}$, see (2.16). From the figure we can see that the highest values of σ_{ef} are in the area of the entrance touching point $P_{touch} = (0.76, 0.25)$, where the velocities have sharp variations.

The plastic deformation starts near the contact area and becomes greater at the following points. It is maximum at the exit point $(x = 1, y = 0.2)$, where the permanent deformation is created. The variation of the viscoplastic strain rate measure $\|\dot{\varepsilon}(t_n)\|_{L^p}^p := \int_{\Omega_{t_n}} 2K\left(3\,\dot{\varepsilon}_{vp}\right)^p$, $p = m+1$, with respect to time for $m \in \{0.15, 0.2, 0.25\}$ is shown in Fig. 3(a). In Fig. 3(b) we present the time variation of the relative velocity measure $\|\mathbf{v}_s(t_n)\|_{L^p}^p := \int_{\Gamma_c} |\mathbf{v}_s(t_n)|^p\, ds$. It should be noted that for all m test cases shown in Fig. 3 the same Δt step size has been used. From the two graphs, we can see that the variations for all test cases show a periodic behavior with a stable amplitude. We can thus consider that the computation has reached the steady-state. As can be seen from the figure, the variation of $\mathbf{v}_s$ for the case of $m = 0.2$ and $m = 0.25$ has similar behavior, with its maximum value occurring on closed time steps.

	Meshes					
Name	C1	C2	M1	M2	F1	F2
Mesh size h	5.02E-03	4.2E-03	3.7E-03	3.01E-03	2.7E-03	2.02E-03

Table 2. The test meshes with the corresponding mesh sizes.

Example 1, $m = 0.2,\ \theta = \frac{\pi}{3}$. In the first example, we start by presenting a short numerical investigation related to the convergence of the numerical results while refining the mesh. We have solved the problem using the meshes given in Table 2 successively. In Fig. 4(a) we plot the variation of the velocity component v_2 on the upper boundary points including the interface points. As we mentioned above, the velocity v_2 is almost zero at the points before the touching entry point P_{touch} of the roller. In a small area after P_{touch} the velocity v_2 increases sharply (in absolute value) and then decreases progressively (decreases almost linearly) reaching zero at the last interface point at the exit. As is expected, the coarse meshes cannot capture the sharp gradient of v_2 efficiently whereas the middle and fine mesh solutions appear to capture them. The solutions of middle and fine meshes have the same behavior without any remarkable differences between them, as can be

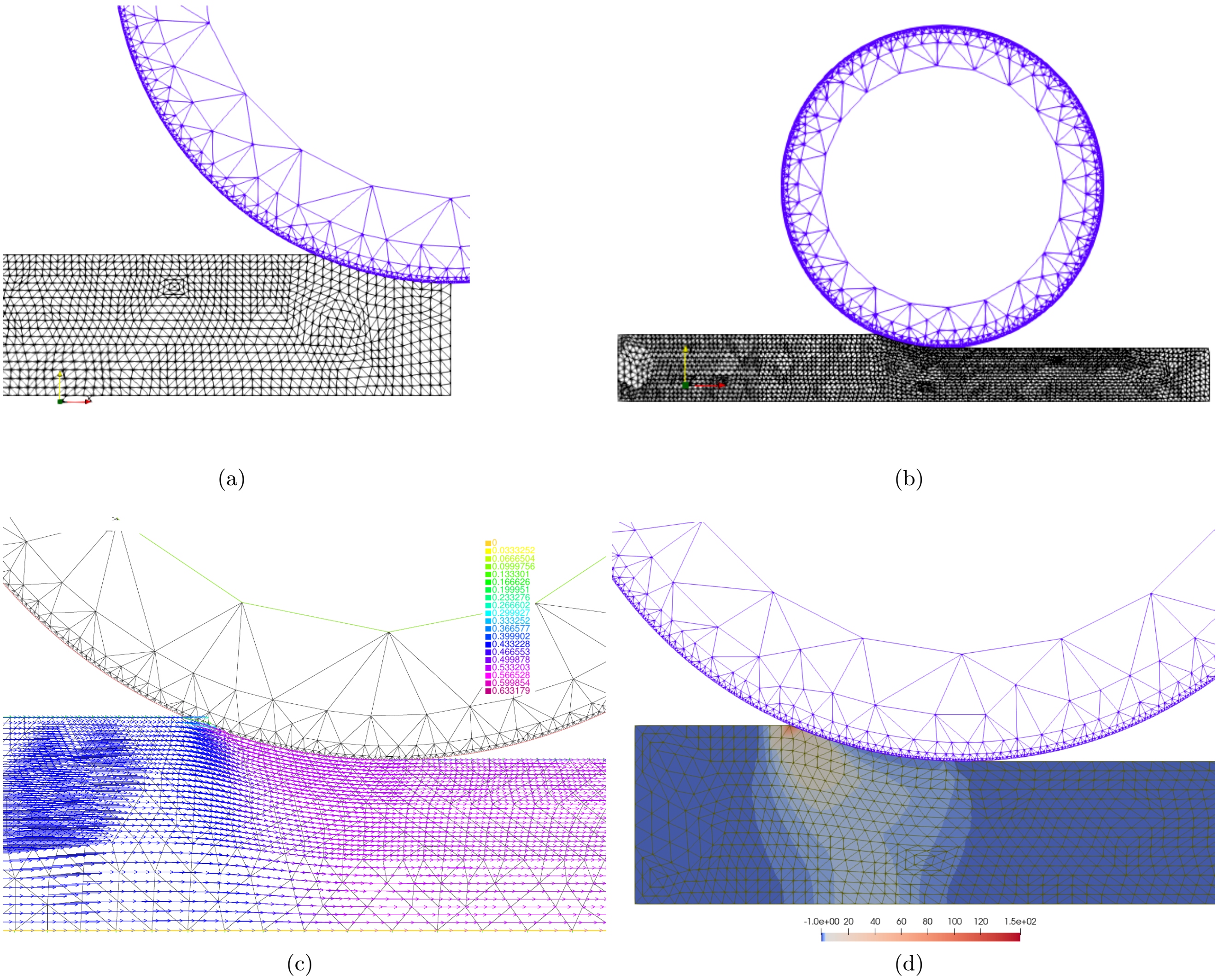

Fig. 2. (a) The initial configuration with a coarse mesh and the touching line, (b) the deformed configuration and the associated mesh at half computational time, (c) focus on the contact area and the velocity contours, (d) the final deformed plate and the distribution of the stress-rate measure.

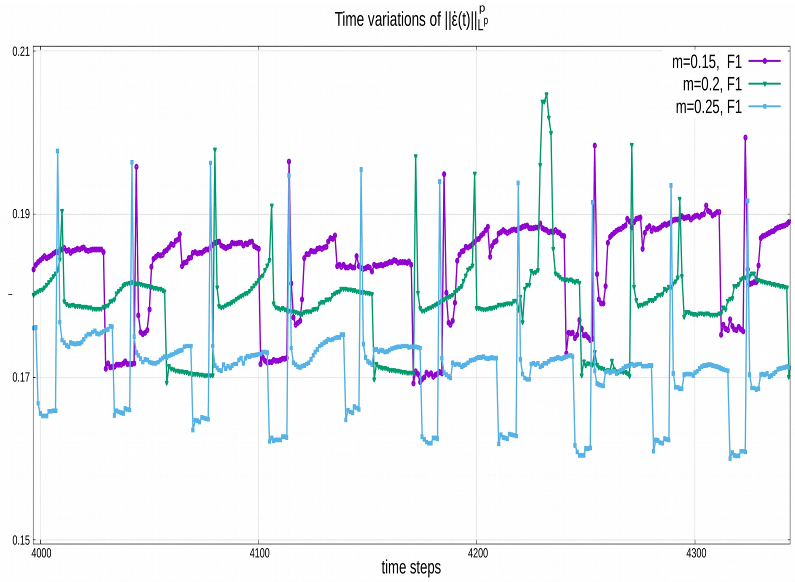

(a)

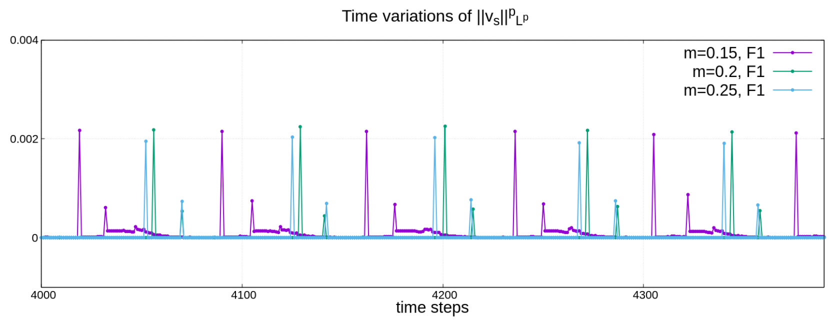

(b)

Fig. 3. Example 1: (a) The variation of the strain rate measure with respect to time, (b) the variation of the relative velocity measure with respect to time.

seen from the plots close to P_{touch}.
The variation of v_1 for the upper boundary has been plotted in Fig. 4(b) from which a good agreement of the numerical solutions is observed. The mesh points before entering into the contact region have a fixed velocity v_1, which is reduced in a small zone close to P_{touch}, compare to Fig. 4(a). After passing through this zone, the points accelerate and leave the contact region with higher velocity.
The variation of $\mathbf{v}_s$ at the upper boundary points for the different meshes are shown in Fig 4(c). Note that for points outside of Γ_C the computation of $\mathbf{v}_s$ is not appropriate. For the initial points at the contact interface the velocity of the plate points is smaller than the velocity of the roller interface points, and thus, we have the negative values of $\mathbf{v}_s$. As the plate moves forward its velocity increases and finally becomes higher than the velocity of the roller. In any mesh test case the relative velocity at the exit points is not so high. We can observe that all the numerical solutions have the same behavior in general. The numerical solution corresponding to the $F2$ mesh captures the variations of $\mathbf{v}_s$ in the neighborhood of P_{touch} in a better manner. At the neutral point the relative velocity between the roller and the plate is zero. The exact location of this point is not a priori known, but it takes its final position at the steady-state. From the numerical computations, the location of the neutral point has been estimated close to the point $P_{neutral} \approx (0.818, 0.22754)$. Fig. 4(d) shows the plots of the relative velocity solutions in a region close to the neutral point. We can observe that all numerical solutions of $\mathbf{v}_s$ are zero in the area of the neutral point.
From a comparison of the graphs above we can say that the numerical solutions computed using the middle and the fine meshes can efficiently capture the variations of the velocity, they have similar behavior, which is not essentially improved when we move to fine meshes. Thus we can say that the middle and fine mesh solutions can provide quite accurate results. In the figures given below, as representative examples, we show only three numerical solutions computed using the associated $C2$, $M2$ and $F2$ meshes.

Fig. 5(a) shows the plots of the tangential stress $\mathbf{T}_\tau \cdot \mathbf{n}_\tau$ over the contact area points. For plotting reasons we devide the results with the number 1.3. From the figure, it can be seen that small numerical oscillations appear close to the first touching point and close to the exit point (0.2,1), due to the steep changes of the velocity and the boundary conditions. We can see that the point where the numerical solution $C2$ crosses the X-axis is located at x=0.83. It is located a little further on the right than the point where the two other numerical solutions cross the X-axis. The fine mesh related solutions cross the X-axis close to the neutral point. The normal stress variations $\mathbf{T}_n \cdot \mathbf{n}$ over the contact points are plotted in Fig. 5(b). The solution related to the $F2$ mesh appears to capture the variations at the entrance points more sharply than the two other solutions. For the next contact points, the behavior of the solutions is similar and for the points after the $P_{neutral}$ the normal stress variations are similar to the variations of $\mathbf{T}_\tau \cdot \mathbf{n}_\tau$. Again, we can see small spurious numerical oscillations at the entrance and exit points. It should be noted here that during the numerical time step computations, the exact locations of the first and last contact points are not fixed and are not a-priori known. These points may be located on the boundaries of the edges or may lie in the interior. So during the computations, it is possible to have mesh elements with one node on the contact line and the other on the free stress boundary parts. This fact is a small reason for the generation of the spurious oscillations.

Example 2, $m = 0.2,\ \theta = \frac{\pi}{6}$. The rolling plate deformation is affected by the radial velocity of the roller, [16], [27]. To examine this we have solved the problem by setting $m = 0.2$, $\theta = \frac{\pi}{6}$ and compared the produced solutions with the solutions of the previous examples. In Fig. 6(a) the profiles of the relative velocities $\mathbf{v}_s$ are plotted along the contact points for the mesh $F1$. As is expected the relative velocity corresponding to $\theta = \frac{\pi}{3}$ is lower, almost double (in negative values) than the velocity of the $\theta = \frac{\pi}{6}$ case. In Fig. 6(b) the profiles of the relative velocities are plotted for the points close to neutral point $P_{neutral}$. As can be seen from the figure, the neutral points have the same locations for both test cases. The velocity of $\frac{\pi}{3}$ is lower for the points on the left of

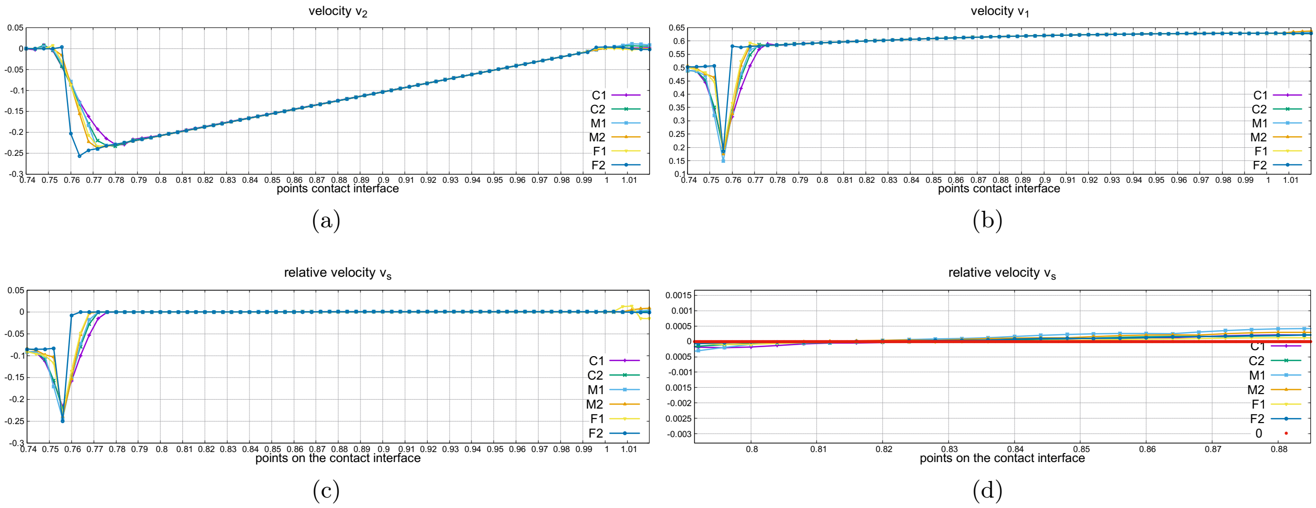

Fig. 4. Example 1: (a) The variations of the v_2 velocity component for all meshes, (b) The velocity v_1 for all meshes, (c) The relative velocity $\mathbf{v}_s$ for all meshes, (d) The relative velocity $\mathbf{v}_s$ around the neutral point $P_{neutral} = (0.818, 0.22754)$, ($\mathbf{v}_s = 0$).

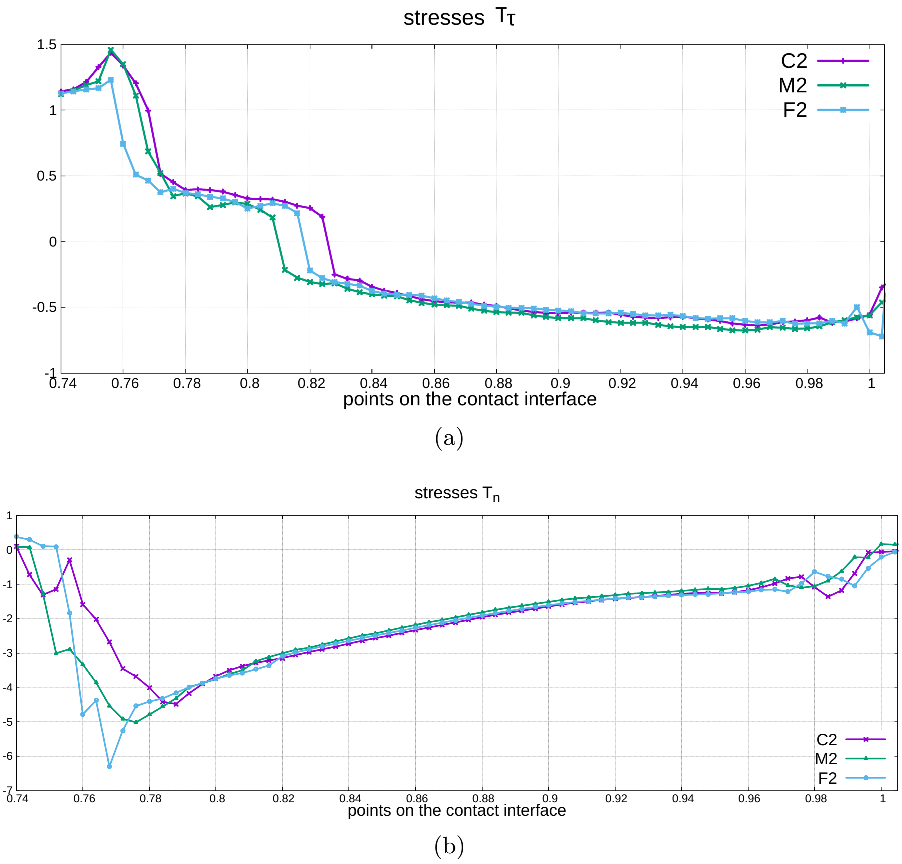

Fig. 5. Example 1: (a) The tangential stress $\mathbf{T}_\tau \cdot \mathbf{n}_\tau$, (b) The normal contact stress $\mathbf{T}_n \cdot \mathbf{n}$.

$P_{neutral}$, and increases after $P_{neutral}$ by progressively double the values as compared to the velocity of the $\frac{\pi}{6}$ case. The variations of the normal stress $\mathbf{T}_n \cdot \mathbf{n}$ and the tangential stress $\mathbf{T}_\tau \cdot \mathbf{n}_\tau$ along the contact interface are shown in Fig. 6(c) and Fig. 6(d) respectively. As we expected the level of the stresses related to the $\theta = \frac{\pi}{3}$ are higher (in absolute values) than the stresses related to the $\theta = \frac{\pi}{6}$ case. It must be noted here that the numerical solutions of $\theta = \frac{\pi}{6}$ show less spurious oscillations at the first and last points on the contact line.

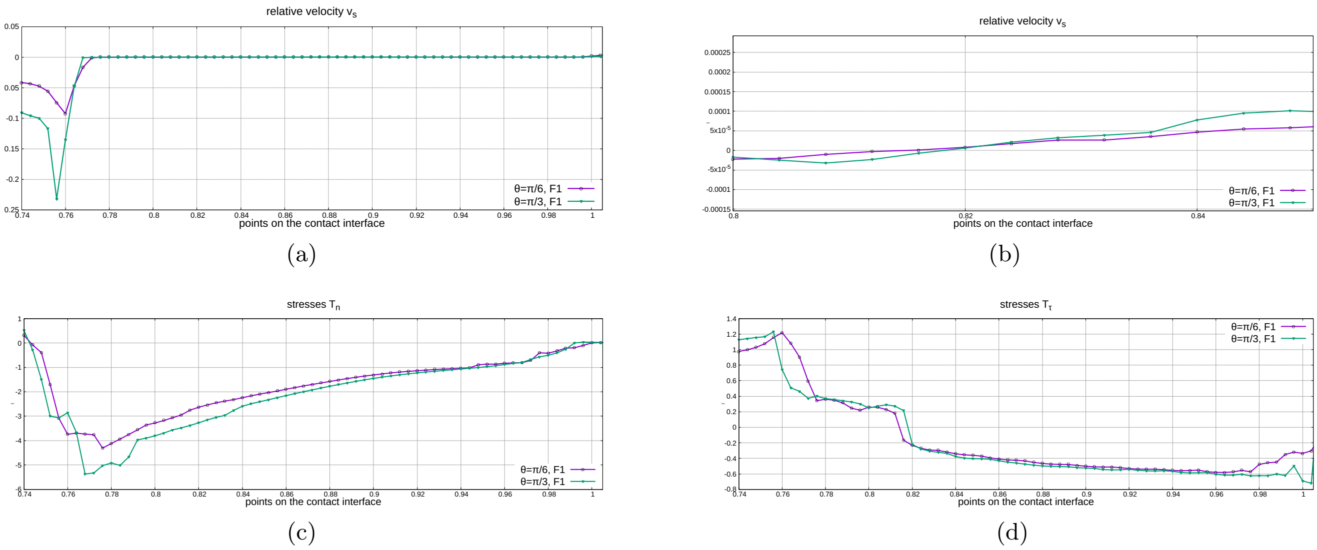

Fig. 6. Example 2: (a) The relative velocities on the whole contact points for $\theta = \dfrac{\pi}{3}$ and $\theta = \dfrac{\pi}{6}$, (b) the variations of the relative velocities in the neighboring of the neutral point, (c) the normal stress $\mathbf{T}_n \cdot \mathbf{n}$, and (d) the tangential stress $\mathbf{T}_\tau \cdot \mathbf{n}_\tau$.

Example 3, $m \in \{0.15, 0.2, 0.25\}$, $\theta = \frac{\pi}{3}$. Rolling is directly affected by the material parameters. In order to investigate this effect we have performed computations with different values for the sensitivity coefficient of the strain rate by setting $m \in \{0.15, 0.25\}$. The computations have been performed by keeping the same speed for the roller $\theta = \frac{\pi}{3}$. The profiles of the corresponding relative velocities for all the cases are given in Fig.7(a). For the points located close to the first touching point, the relative velocity decreases (in absolute values) when we increase the exponent m, see for example the $m = 0.25$ test case. For the points slightly to the right of the touching point, $\mathbf{v}_s$ increases by almost the same rate for all m-test cases. In Fig. 7(b) the variations of the relative velocities close to $P_{neutral}$ are plotted. It can be seen that $\mathbf{v}_s$ of the test case $m = 0.15$ grows faster than the other two cases and crosses the $X-$axis at a point which is located slighlty more to the left of $P_{neutral}$, (note here that $P_{neutral}$ is the neutral point which corresponds to the $m = 0.2$ test case). For the rest of the boundary points it remains greater than the other two velocities. The relative velocity related to the $m = 0.25$ case crosses the X-axis at a point very close to $P_{neutral}$ and has a similar behavior to the relative velocity of the $m = 0.2$ test case.
Fig. 7(c) shows the normal stresses over the contact points. For the first points the normal stress values of the $m = 0.15$ case are higher (in absolute value) than the other test cases. For the rest of the points the stress curves have similar behavior with only small differences. The plot line corresponding to the $m = 0.25$ case has less oscillations as compared to the other two lines. Finally, the curves of the tangential stresses are given in Fig. 7(d). The values related to the $m = 0.15$ case are higher (in absolute values) as compared to the other two cases. The position of the neutral point has moved slightly on the left compared to the curves for the other two cases, compare also with Fig. 7(b). As expected from Figs. 7(a) and (b), the behavior of the tangential stresses for the $m = 0.2$ and $m = 0.25$ cases is observed to be similar.

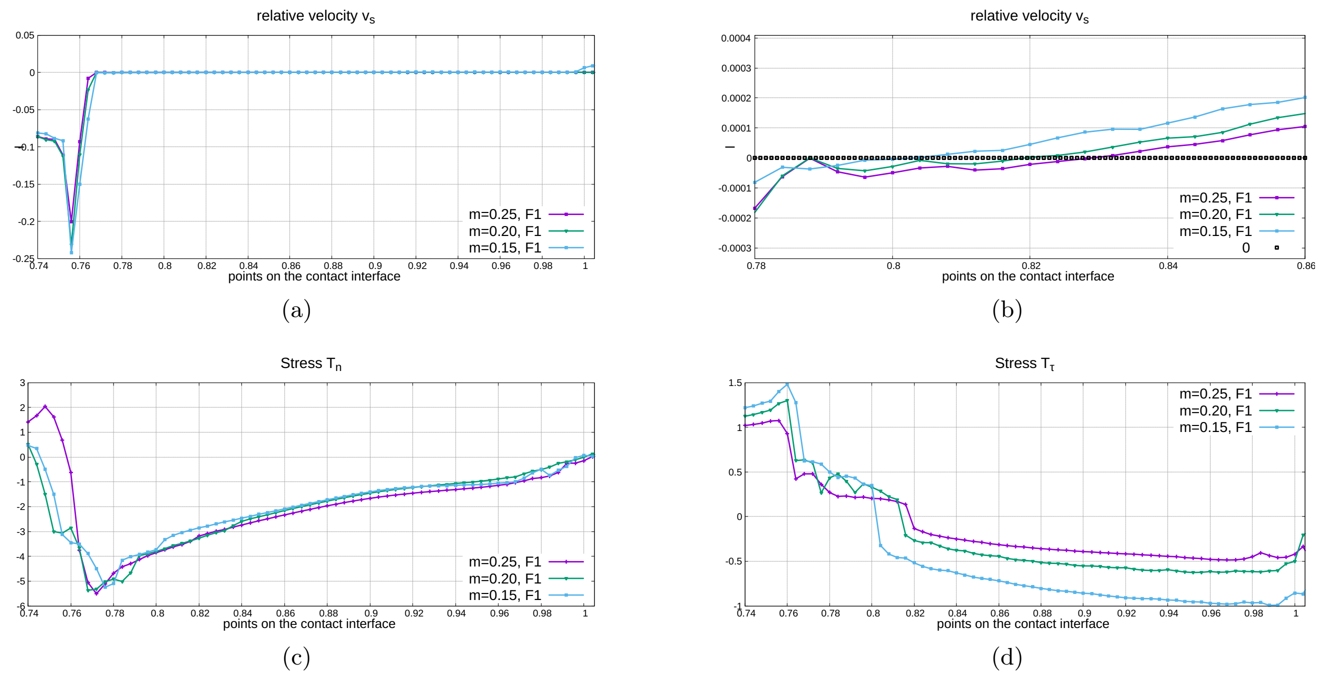

Fig. 7. Example 3: (a) the relative velocities for the three $m-$test cases, (b) the relative velocities close to neutral point, (c) the normal stresses $\mathbf{T}_n \cdot \mathbf{n}$, (d) the tangential stress $\mathbf{T}_\tau \cdot \mathbf{n}_\tau$.

Conclusions

In this work, viscoplastic mathematical models for the hot rolling process of metal-forming are described in detail under the assumption that elastic effects are negligible. After deriving the basic constitutive law, the bilateral contact conditions and a viscoplastic type friction law are discussed. The associated system of the equilibrium equations has been presented giving special emphasis on the construction of the penalty terms that can incorporate the boundary constraints of the inlet/outlet velocity as well the bilateral contact conditions in the system. A standard finite element scheme with continuous Taylor-Hood polynomial spaces, together with an explicit time approach for updating the configuration, have been applied for discretizing the equilibrium system. Innovation in this work was the estimation of the friction parameter, a_f, through the proof of stability bounds for the finite element scheme. Moreover, several important aspects, which arise during the implementation of the algorithm for solving the rolling problems, are discussed. The appropriateness of the whole approach has been investigated by performing several numerical tests that concern the estimation of the position of the neutral point, the magnitude of the normal/tangential stresses and the variations of the relative tangential velocity. The numerical results show that the choice of the strain rate sensitivity coefficient and the roller speed affects the magnitude of the normal and tangential stresses and the variations of the relative velocity, but not essentially the position of the neutral point.

In many realistic contact problems with viscoplastic materials, more detailed modeling of the interface friction phenomena and the dependency of the friction coefficient, a_f, on other variables such as temperature and surface roughness is required. Moreover, more advanced finite element methodologies and efficient implementation of the algorithm, for example, curved meshes in a parallel environment for fast performance computing, is necessary for producing more accurate numerical simulations.

Acknowledgements

This work has been supported by the project COMET K2 XTribology, No 849109, Project grantee: Excellence Center for Tribology, and by the JKU-LIT project LIT-2017-4-SEE-004. The author would like to thank Dr M. Jech and Dr. G. Vorlaufer for useful discussions.

References

1. R. A. Adams and J. J. F. Fournier. *Sobolev Spaces*, volume 140 of *Pure and Appled Mathematics*. ACADEMIC PRESS-imprint Elsevier Science, Amsterdam, Netherlands, second Edition edition, 2003.
2. T. Belytschko, W. K. Liu, B. Moran, and K. I. Elkhodary. *Nonlinear finite elements for continua and structures*. A John Wiley and Sons, West Sussex, PO19 8SQ, United Kingdom, 2nd edition, 2008.
3. S.C. Brener and L. R. Scott. *The mathematical Theory of Finite Element Methods*, volume 15 of *Texts in Applied Mathematics*. Springer-Verlag New York, third Edition edition, 2008.
4. E.A de Souza Neto and D. R.J. Owen D. Perić. *COMPUTATIONAL METHODS FOR PLASTICITY, THEORY AND APPLICATIONS*. A John Wiley and Sons, Ltd, Publication, West Sussex, PO19 8SQ, United Kingdom, 1st edition, 2008.
5. X. Duan and T. Sheppard. Three dimensional thermal mechanical coupled simulation during hot rolling of aluminium alloy 3003. *International Journal of Mechanical Sciences*, 44(10):2155 – 2172, 2002.
6. L. Fourment, J. L. Chenot, and K. Mocellin. Numerical formulations and algorithms for solving contact problems in metal forming simulation. *International Journal for Numerical Methods in Engineering*, 46:1435 – 1462, 1999.
7. M. Fuchs and G. Seregin. *Variational methods for problems from plasticity theory and for generalized Newtonian fluids*, volume 1749 of *Lecture notes in mathematicsSIAM studies in applied mathematics*. Springer-Verlag, Berlin-Heidelberg, 2000.
8. V. B. Ginzburg and R. Ballas. *Flat Rolling Fundamentals*. Manufacturing Engineering and Materials Processing. CRC Press, Taylor and Francis group, 2000.
9. R. Glowinski, J. L. Lions, and R. Trémoliéres. *Numerical analysis of variational inequalities*, volume 8 of *Studies in mathematics and its applications*. Elsevier Amsterdam North-Holland Pub. Co, New York, U.S.A., 1981.
10. P. Hartley, I. Pillinger, and editors C. Sturgess. *Numerical Modeling of Material Deformation Processes, Research, Developement and Applications*. Springer-Verlag, London, 1992.
11. J. Haslinger, M. Miettinen, and P. D. Panagiotopoulos. *Finite Element Method for Hemivariational Inequalities*, volume 35 of *Nonconvex Optimization and Its Applications*.
12. Y. J. Hwu and J. G. Lenard. A Finite Element Study of Flat Rolling. *Journal of Engineering Materials and Technology*, 110(1):22–27, 1988.
13. I.V.Samarasekera. Hot Rolling. In K.H. J. Buschow and et. al., editors, *Encyclopedia of Materials: Science and Technology*. Elsevier, U. K., 2nd edition.
14. C. Johnson. *Numerical Solution of Partial Differential Equations by the Finite Element Method*. Cambridge University Press, 1988.
15. K.L. Johnson. *Contact Mechanics*. Cambrige University Press, Cambrige, U. K., 1st edition, 1987.
16. J. J. Kalker. *Three-Dimensional Elastic Bodies in Rolling Contact*. Springer-Verlag, Netherlands, 2nd edition, 1990.
17. S. Kobayashi, S.I. Oh, and T. Altan. *Metal Forming and the Finite-Element Method*. Oxford Series on Advanced Manufacturing. Oxford University Press, New York, 1st edition, 1989.
18. J. Lenard. *Primer on Flat Rolling*. Nonconvex Optimization and Its Applications. Oxford U.K., 2nd edition.
19. G. J. Li and S. Kobayashi. Rigid-Plastic Finite-Element Analysis of Plane Strain Rolling. *Journal of Engineering for Industry*, 104(1):55–63, 1982.
20. Alberto Murillo-Marrodán, Eduardo Garcia, and Fernando Cortés. A study of friction model performance in a skew rolling process numerical simulation. volume 17, pages 569–582, 2018.
21. Kikuchi N and Oden J. T. *Contact problems in elasticity: A study of variational inegualities and finite element methods*. SIAM studies in applied mathematics. SIAM, Philadelphia, USA, 1988.
22. A. Ösner. *Elasto-Plasticity of Frame Structure Elements*. Springer-Verlag, Berlin Heidelberg, 1st edition, 2014.
23. E. Oñate and O.C. Zienkiewicz. A viscous shell formulation for the analysis of thin sheet metal forming. *International Journal of Mechanical Sciences*, 25(5):305 – 335, 1983.
24. M. Rappaz, M. Bellet, and M. Deville. *Numerical Modeling in Materials Science and Engineering*, volume 32 of *Springer Series in Computational Mathematics*. Springer-Verlag, Berlin-Heidelberg, 2003.
25. A. B. Richelsen. Viscoplastic analysis of plane-strain rolling using different friction models. *Int. J. Mech. Sci.*, 33(9):761–774, 1991.
26. J. C. Simo and T.J.R. Hughes. *Computational Inelasticity*. (Springer-Verlag, NewYork, Inc., 175 Fifth Avenue, 10010, USA, 1st edition, 1998.
27. J. Synka, A. Kainz, R. Maringer, and A. Obereder. Numerical analysis of a new Eulerian-Langrangian finite element method applied to steady-state hot rolling processes. *International Journal for Numerical Methods in Engineering*, 62:616 – 638, 2005.
28. S. Turek. *Efficient Solvers for Incompressible Flow Problems*, volume 6 of *Lecture Notes in Computational Science and Engineering*. Springer-Verlag, Berlin Heidelberg, 1 edition.
29. H Wennerström, A. Samuelsson, and K. Mattiasson. Finite element method for sheet metal strechinglow formulation for numerical solution of forming processes. In Pittman JFT et al, editor, *Numerical analysis of forming processes*. John Wiley, 1984.

30. S. Werner, M. Stingl, and G. Leugering. Model-based control of dynamic frictional contact problems using the example of hot rolling. *Computer Methods in Applied Mechanics and Engineering*, 319:442 – 471, 2017.
31. P. Wriggers. *Computational Contact Mechanics.* Springer-Verlag, Berlin-Heidelberg, 2006.
32. P. Wriggers. *Nonlinear Finite Element Methods.* Springer-Verlag, Berlin-Heidelberg, 2008.
33. Z. Wusatowsky. *Fundamentals of Rolling.* Pergamon Press,, Oxford, U. K., 1969.
34. S. Xiong, J.M.C. Rodrigues, and P.A.F. Martins. Application of the element free galerkin method to the simulation of plane strain rolling. *European Journal of Mechanics - A/Solids*, 23(1):77 – 93, 2004.
35. S.H. Zhang, G.L. Zhang, J.S. Liu, C.S. Li, and R.B. Mei. A fast rigid-plastic finite element method for online application in strip rolling. *Finite Elements in Analysis and Design*, 46(12):1146 – 1154, 2010.
36. O. C. Zienkiewicz. Flow formulation for numerical solution of forming processes. In Pittman JFT et al, editor, *Numerical analysis of forming processes.* John Wiley, 1984.
37. O. C. Zienkiewicz, P. C. Jain, and E Oñate. Flow of solids during forming and extrusion: some aspects of numerical simulation. *International Journal of Solids and Structures*, 14(1):15 – 38, 1978.

Latest Reports in this series

2009 - 2018

[..]

2019

2019-01	Helmut Gfrerer and Jiří V. Outrata *On a Semismooth* Newton Method for Solving Generalized Equations*	April 2019
2019-02	Matúš Benko, Michal Červinka and Tim Hoheisel *New Verifiable Sufficient Conditions for Metric Subregularity of Constraint Systems with Applications to Disjunctive Programs*	June 2019
2019-03	Matúš Benko *On Inner Calmness*, Generalized Calculus, and Derivatives of the Normal-cone Map*	October 2019
2019-04	Rainer Schneckenleitner and Stefan Takacs *Condition number bounds for IETI-DP methods that are explicit in h and p*	December 2019
2019-05	Clemens Hofreither, Ludwig Mitter and Hendrik Speleers *Local multigrid solvers for adaptive Isogeometric Analysis in hierarchical spline spaces*	December 2019

2020

2020-01	Ioannis Toulopoulos *Viscoplastic Models and Finite Element Schemes for the Hot Rolling Metal Process*	February 2020

From 1998 to 2008 reports were published by SFB013. Please see
`http://www.sfb013.uni-linz.ac.at/index.php?id=reports`
From 2004 on reports were also published by RICAM. Please see
`http://www.ricam.oeaw.ac.at/publications/list/`
For a complete list of NuMa reports see
`http://www.numa.uni-linz.ac.at/Publications/List/`